Thermal Stability of Nano-Structured Selective Emitters for Thermophotovoltaic Systems

by

Héon Ju Lee

B.S., Korea University (2001)

M.S., Texas A & M University (2003)

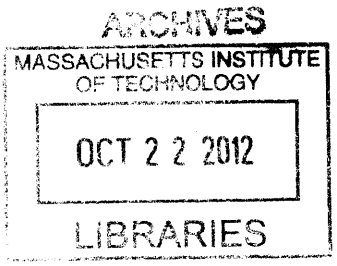

Submitted to the Department of Mechanical Engineering
in Partial Fulfillment of the Requirements for the Degree of

Doctor of Philosophy

at the

MASSACHUSETTS INSTITUTE OF TECHNOLOGY

August 2012
[SEPTEMBER 2012]

Signature of Author .....
Department of Mechanical Engineering
August 10, 2012

Certified by .....
Sang-Gook Kim
Professor of Mechanical Engineering
Thesis Supervisor

Accepted by.....
David E. Hardt
Chairman, Department Committee on Graduate Students

Thermal Stability of Nano-Structured Selective Emitters for Thermophotovoltaic Systems

by

Heon Ju Lee

Submitted to the Department of Mechanical Engineering
Submitted on August 24, 2012 in Partial Fulfillment of the
Requirements for the Degree of
Doctor of Philosophy

Abstract

A fundamental challenge in solar-thermal-electrical energy conversion is the thermal stability of materials and devices at high operational temperatures. This study focuses on the thermal stability of tungsten selective emitters for thermophotovoltaic (TPV) systems which are anticipated to enhance the conversion efficiency.

Selective emitters, 2-D photonic crystals, are periodic micro/nano-scale structures that are designed to affect the motion of photons at certain wavelengths. The structured patterns, however, lose their structural integrity at high temperatures, which disrupt the tight tolerances required for spectral control of the thermal emitters.

Through analytical studies and experimental observations, the failure modes of tungsten 2-D photonic crystal are indentified. There were four major mechanisms of thermal degradation by which micro/nano-scale structures change their geometry when heated: grain growth and recrystallization, oxidation, surface diffusion, and evaporation.

A novel idea of flat surface tungsten photonic crystal (FSTPC) was proposed and was validated by theoretical modeling and by experiments. Pre-annealing or using single crystalline tungsten will prevent the grain growth. A thin layer of diffusion barrier will prevent oxidation and/or evaporation and maintain the optical performance. By filling in the micro/nano-scale cavities with a damascened IR transparent ceramic, the surface of the emitter will have negligible second derivative of the curvature, and thus eliminates the surface diffusion even at high temperatures.

Accelerated tests on silicon-based 2-D photonic crystal show that the micro/nano-scale structures on the silicon surface survive for at least 100 hours at 400 °C, homologous temperature of 0.4, which is equivalent temperature of 1200 °C for tungsten. Based on a scale-accelerated failure model, the life time of the Flat Surface Tungsten Photonic Crystal (FSTPC) is estimated to be at least 40 years at 800 °C.

Thesis Supervisor: Sang-Gook Kim

Acknowledgments

First and foremost, I thank God for giving me the strength and guidance in this long, arduous passage. Without His grace, I would not have had the wisdom and the ability to face this challenge.

To be able to step strong and smooth in this journey, I have also been supported and supervised by many people. Very special thanks are due to Prof. Sang-Gook Kim, for without his motivating encouragement I would not have been able to embark on this study. Prof. Kim is the one professor/teacher who truly has made a difference in my life. He has provided me with direction and technical support, and was a great mentor. I owe him my eternal gratitude, but doubt that I will ever be able to convey my appreciation fully. Very special thanks are also due to Prof. Jung-Hoon Chun for clarifying the research topic and keeping me always focused on key issues, and to Dr. Nannaji Saka for numerous discussions on surface engineering and for guidance in thesis writing.

Thanks to Dr. Stephen Bathurst and Dr. Michael Ghebrebrhan for assisting me in analysis and modeling. Thanks are also due to Prof. Marin Soljacic and Dr. Veronika Rinnerbauer. Without the micro/nano-scale pattern masks (by interference-lithography) furnished by them, I could not have finished the experiments in time.

Finally, I gratefully acknowledge the support of my family throughout my entire life. In particular, I must acknowledge my wife and best friend, Hyun, without whose love, encouragement and commitment, I would not have completed this thesis.

Contents

List of Figures

List of Tables

Chapter 1

Introduction

1. Solar Thermophotovoltaic (STPV) Systems

1.1 Photovoltaics (PV)

Photovoltaics (PV) are energy conversion systems that can directly convert solar radiation into electricity. The first demonstrated photovoltaic device was a Pt electrode coated AgCl cell, which was immersed into an acidic solution, by Becquerel in 1839 [1]. The next research reported was the photoconductive effect on selenium (Se) in 1883. This research led to the first thin-film solar cell fabricated with Se in 1883 by Fritts [2]. Until the 1940's, Se, Cu_2O and Tl_2S were the absorbing layers with metal electrodes. The first semiconductor p–n junction solar cell was introduced by Russell Ohl in 1941 [3]. From that time on, most photovoltaic solar cells have been fabricated based on silicon p-n junctions.

1.1.1 p-n junction for PV

The principle of a p-n junction can be explained with Figure 1.1 [4]. In a pure semi-conductor (intrinsic semiconductor), incoming photon with enough energy can promote the electron from the *valence band* to become a free electron in the *conduction band*. The difference in these two energy levels is called the *band-gap*. It is also the minimum energy required for generating free electrons. This band-gap varies from material to material and with temperature. However, in an intrinsic semiconductor, the promoted electrons re-combine with the holes resulting in no electric current. By doping the foreign atoms in regular crystal lattice, we can push up (p-type) or pull down (n-type) the overall energy levels. By joining these two layers, a charge-free depletion zone can be obtained. This junction can create a slope in the energy bands and allow excited electrons to "roll down" into a lower energy band rather than instantly re-combine with a hole. This can allow the continuous generation of electric current.

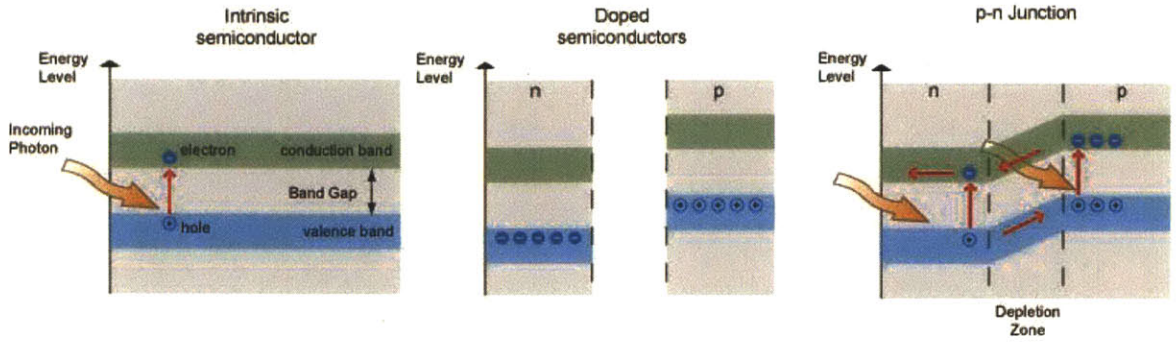

Figure 1.1 Energy levels of on intrinsic semiconductor, p-type and n-type semiconductors, and a p-n junction. Each material has unique value of band-gap [4].

1.1.2 Limits of the single p-n junction PV

However, this p-n junction solar cell has a theoretical limit, known as Shockley-Queisser (SQ) limit. It was first calculated by William Shockley and Hans Queisser in 1961 [5]. A solar cell's energy conversion efficiency is defined as the percentage of power converted from sunlight to electricity under "standard test conditions (STC)." The STC conditions are noon in spring and autumn equinoxes in the continent US with the surface of the solar cell facing directly normal to the sun. Most of solar panel manufacturers use this STC. They put the solar panels in a flash tester in their factory that has been calibrated to deliver the equivalent of 1000 watts per square meter of sunlight intensity, hold a cell temperature of 25 ^{o}C, and assume an air mass of 1.5 (AM 1.5). This value of 1000 W/m^2 is the measured nominal full sunlight intensity on a bright clear day, which is defined as '1 sun intensity' or shortly '1 sun.' The air mass coefficient (AM), or atmosphere thickness, defines the direct optical path length through the Earth's atmosphere, expressed as a ratio relative to the path length vertically upwards. "AM1.5" is almost universal when characterizing terrestrial power-generating panels. That is because many of the world's major population centers lie in not normal but temperate latitudes. 1.5 atmosphere thickness, corresponds to a solar zenith angle of z = 48.2°.

Figure 1.2 is the solar spectrum at 1 sun and AM1.5 condition, 930 W/m^2. A silicon-based PV cells can only use photons with energies larger than the band-gap of 1.1eV, and hence wastes a large fraction of useful energy with photons below the band-gap. Furthermore, only a

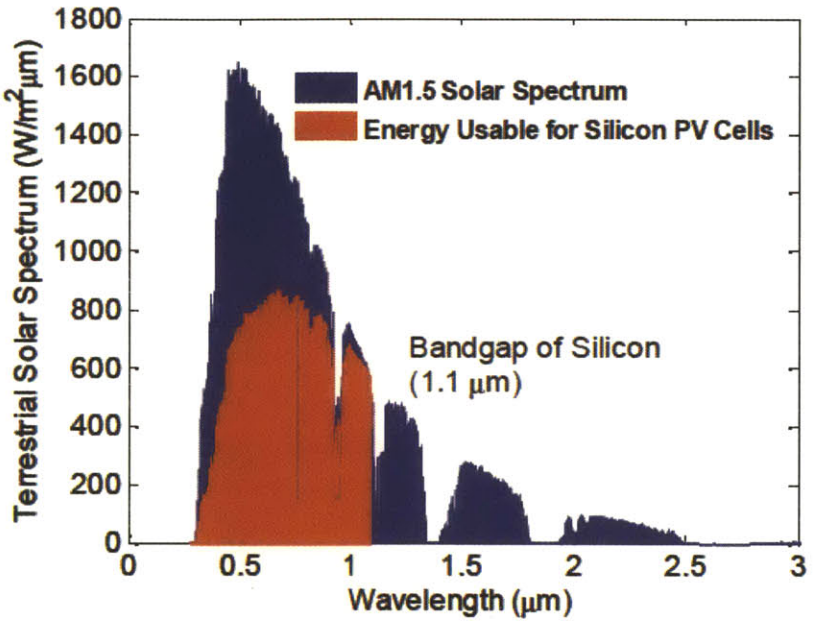

Figure 1.2 Solar insolation at AM1.5. Red regions are energy usable for Si-based PV cells. The Blue regions are energy wasted as heat [6].

fraction of the photon energy above the band-gap is useful. Therefore, p-n junction solar cell loses the radiated energy by heat dissipating and photons passing through the solar cells. It is reported that for non-concentration condition (1 sun), the modern SQ limit has a maximum efficiency of 33% for any type of single-junction solar cell.

There are four efficiency losses in p-n junction solar energy conversion. First, the average energy of the photons is much higher than the band-gap. The excess energy is lost as heat. Second, photons with energy below the band-gap that are not useful for electron-hole generation (Figure 1.2) and only the fraction of photons with energy above the gap is useful. Third, the extracted voltage, reflecting the electrochemical potential energy difference between the two electrodes, is less than the band-gap. Finally, the excited electrons re-combine with holes.

Although solar cell production efficiencies vary with the band-gap of the semiconductor materials and operation temperature, the best efficiency of single junction silicon solar cell in production to date is 24% at the cell level and 20% at the module level as reported by SunPower

in March 2012. In a laboratory, the record high solar cell efficiency is held by the University of New South Wales in Sydney, Australia at 25% [7].

1.1.3 Third generation photovoltaic cells

p-n junction semiconductor photovoltaic cells are the first generation PV cells. For reducing the cost of the first generation cells, thin film technologies have been employed, which are considered the second generation PV cells. The third generation PV cells are solar cells that are potentially able to overcome the Shockley–Queisser limit of 31% (1 sun) – 41% (concentrated) power conversion efficiency of single junction solar cells. The most common third-generation systems include multi-layer ("tandem") cells made of amorphous silicon or gallium arsenide, with more theoretical developments including frequency conversion, hot-carrier effects and other multiple-carrier ejection.

1.1.4 Multi-junction photovoltaic cells

Among third generation Photovoltaic cells, multi-junction photovoltaic cells achieved significant improvements for higher efficiency. The "band-gap engineering" uses monolithic stacking of multiple cells on top of one another, so that each cell efficiently converts a relatively narrow range of photon energies suited to its band gap, Figure 1.3 [8]. The maximum conversion efficiency for multi-junction solar cells reported in July 2012 is about 30 % (commercially available, Emcore) for 1 sun illumination, and it improves to around 40 % under concentrated sunlight.

However, as of this year, the cost of multi-junction solar cells is still too high to use except for specialized applications. The high cost mainly results from the manufacture of complex structures and the high price of materials. The fabrication process for multi-junction solar cell uses techniques similar to semiconductor device fabrication, usually metalorganic vapor phase epitaxy (continuous chemical vapor deposition), which involves very high energy consumption per product volume [9].

At present, many research directions are being pursued to improve either one or several of the above factors simultaneously, almost exclusively from the PV cell side. Not only with multi-junction solar cells [10], multiple-exciton generation [11] and hot electron cells [12]

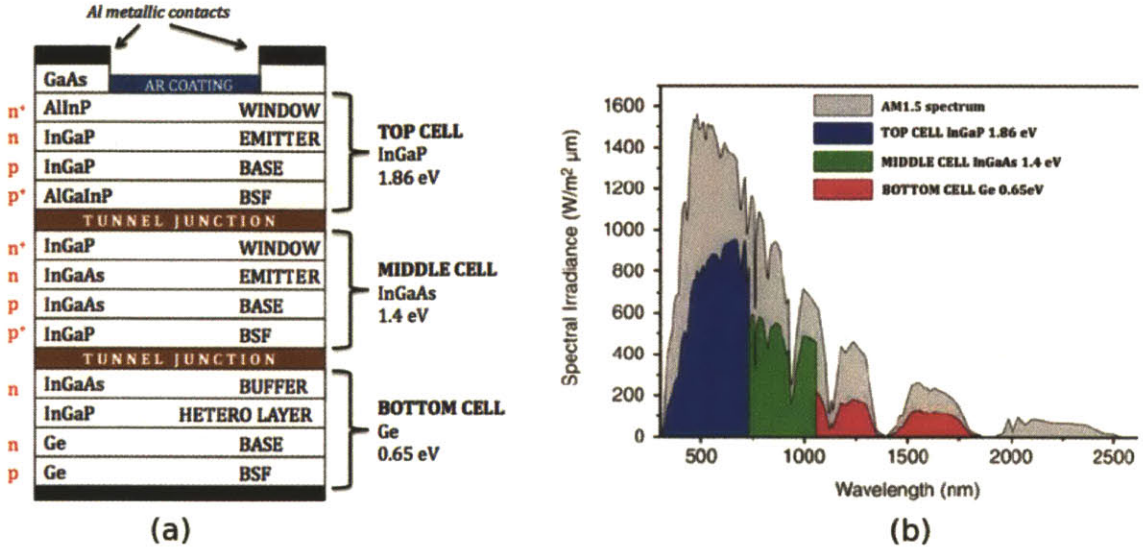

Figure 1.3 (a) Structure of a Multi-junction solar cell. There are six important types of layers: p-n junctions, back surface field (BSF) layers, window layers, tunnel junctions, anti-reflective coating and metallic contacts, (b) Graph of spectral irradiance (E) vs. wavelength (λ) over the AM 1.5 solar spectrum, together with the maximum electricity conversion efficiency for every junction as a function of the wavelength [8].

mainly aimed at minimizing energy losses from radiated energy which exceed the band-gap energy. Among these approaches, three-junction cells have achieved 40.8 % while the theoretical maximum efficiency of an infinite number of junction PV cells is 86.8 %. The rest of the above-mentioned PV cells, which are usually called the third generation PV cells, are still in the conceptual stage. Figure 1.4 shows the history of best up–to-date solar conversion efficiencies reported from 1976 to July 2012 [13].

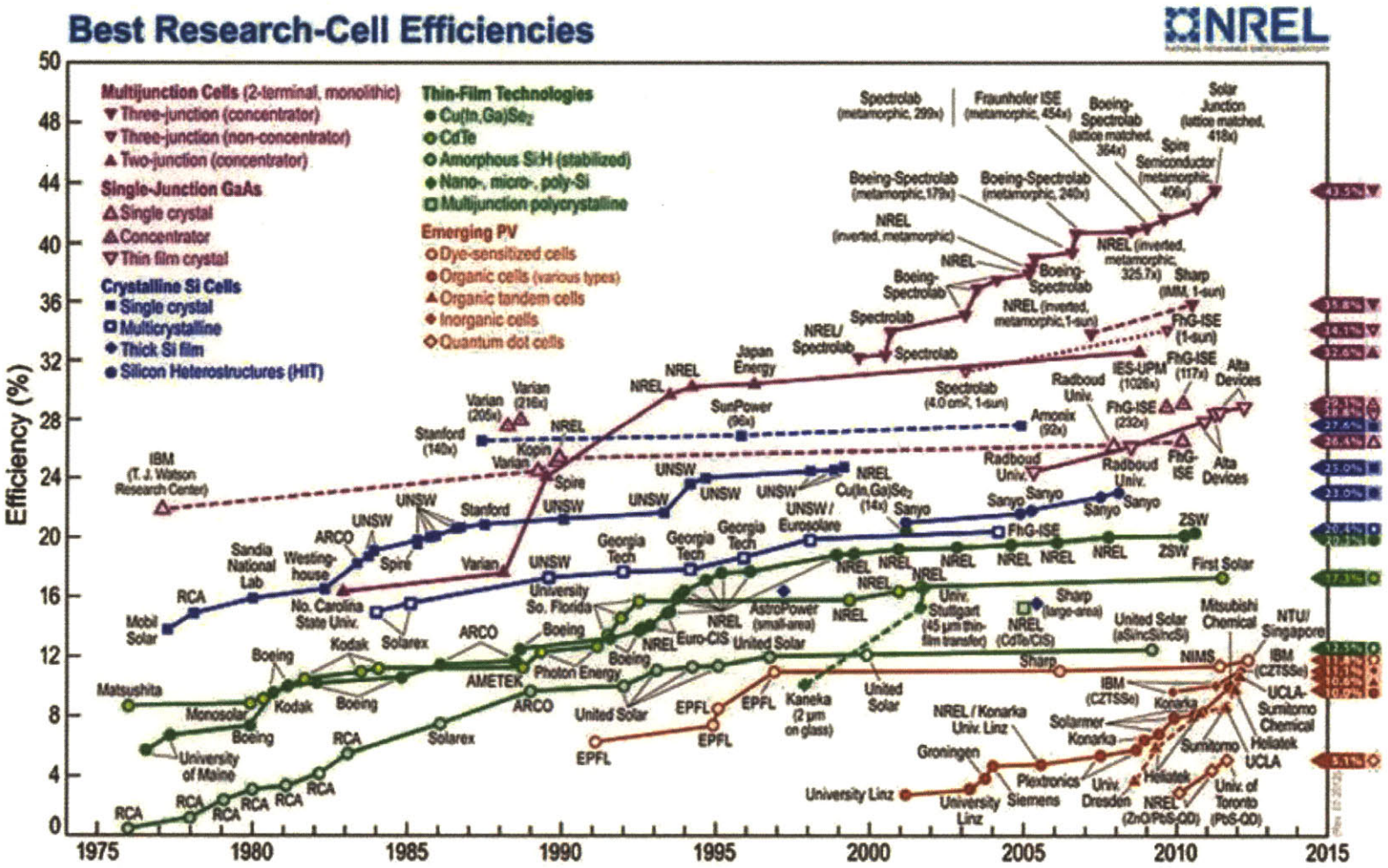

Figure 1.4 Conversion efficiencies of best research solar cells worldwide from 1976 through 2012 for various photovoltaic technologies. Efficiencies determined by certified agencies/laboratories [13].

1.2. Solar Thermophotovoltaic Systems

1.2.1 Concept of S-TPV systems

Solar Thermo Photo Voltaic (S-TPV) cells are also one of the third generation solar cells [14, 15]. However, S-TPVs pursue a very different strategy to increase the solar-to-electricity energy conversion efficiency based on the same photovoltaic principle. Rather than focusing on the PV cell, the emphasis is shifted to controlling the spectra of the photons entering the PV cell. Figure 1.5 shows the strategy to achieve this effect [16, 17]. Broadband solar insolation is first absorbed by the surface, which heats the absorber to 1000-2000 ^{o}C. On the other side of the absorber is the emitter, which re-radiates photons that are optimized to match the photovoltaic cell.

In detail, as it can be seen from Figure 1.5 (a), the solar insolation has large peak in near IR and visible wave-length. However, the GaSb photovoltaic cell shows sharp drop on its quantum efficiency at 1.7 μm (1.1 μm for Si PV cells), Figure 1.5 (d). The specially designed selective absorber can absorb the most of the wave-length from the sun light, Figure 1.5 (b), and then transfer the concentrated energy to the selective emitter in a form of thermal energy. This heat energy then emits to PV cells only with tailored range of wave-length which is matching with PV cells' maximum quantum efficiency. In this way, the system can use the most of the energy from the sun and can achieve higher conversion efficiency.

The theoretical maximum efficiency of such solar TPV converters is 85.4 % for full concentration and 54% with no-concentration [18, 19]. These numbers came from the simple calculation of assuming black absorber, no heat losses, adiabatic and reversible. It, also, assumed that every photon has exactly the amount of band-gap for PV cells and excessive energy recycled 100 %. By applying the Stepan-Boltzman's law and the Carnot efficiency, absorber efficiency (η_{abs}), cell efficiency (η_{cell}), and system efficiency (η_{TPV}) can be written as:

$$\eta_{abs} = 1 - \frac{\pi}{\Omega_S}\frac{T_A^4}{T_S^4} \tag{1.1}$$

$$\eta_{cell} = 1 - \frac{T_o}{T_A} \tag{1.2}$$

$$\eta_{TPV} = \left(1 - \frac{\pi}{\Omega}\frac{T_A^4}{T_S^4}\right)\left(1 - \frac{T_o}{T_A}\right) \tag{1.3}$$

where Ω is solid angle, which is Ω_s = 6.8 x 10^{-5} for non-concentrated light and $\Omega = \pi$ for maximum concentration. T_A is absorber's temperature, T_s is the temperature of solar radiation and T_o is the PV cell's temperature. For a given condition, T_o = 300 K and T_s = 6000 K, the maximum TPV system efficiency can be obtained from Equation (1.3) at T_A = 2544 K as 85.4 %.

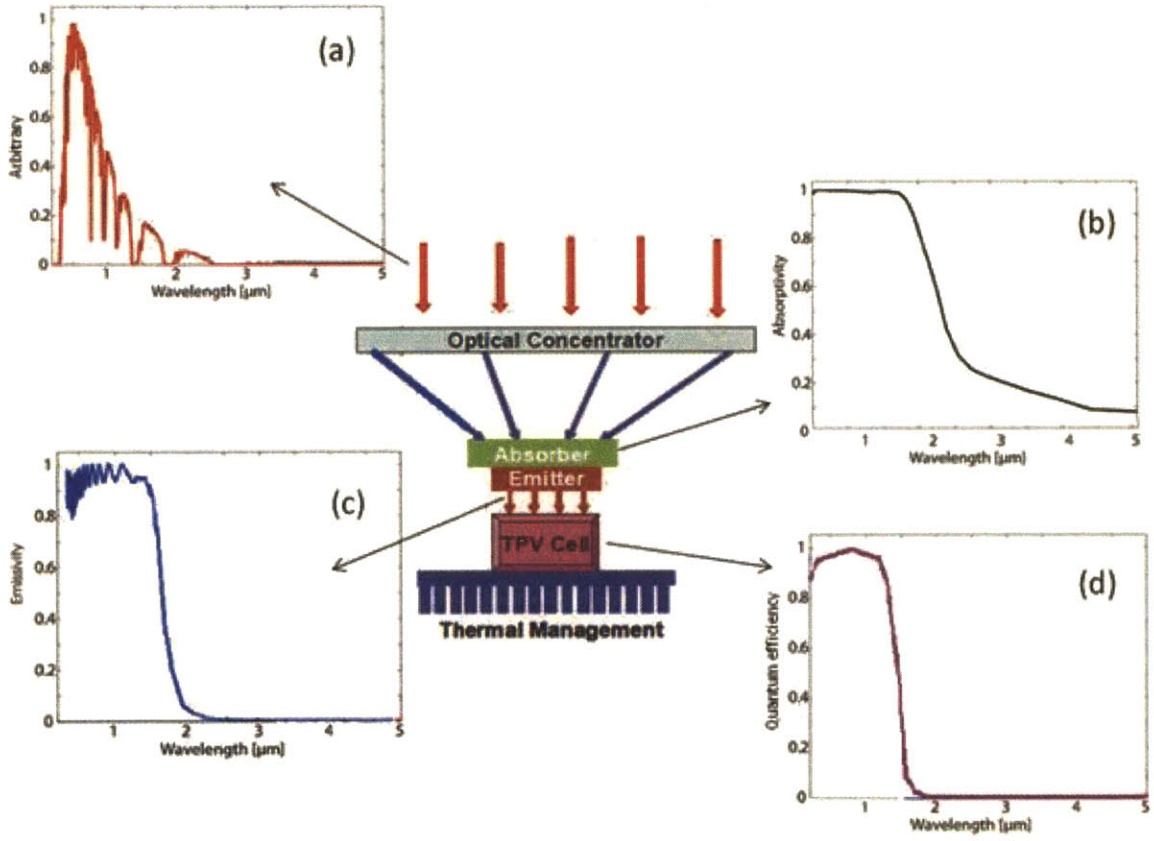

Figure 1.5: Illustration of a solar thermophotovoltaic (TPV) converting system. Broadband solar insolation (inset a) heats up a selective absorber (inset b), which conducts heats to a selective emitter (inset c), which emits in a narrow band (inset d) into a PV cell to generate electricity. Theoretical limit-efficiency of a single junction solar TPV converter is 85.4% [18]. The figure redrawn based on solar TPV system from [17].

This is very close to that of multi-junction cells with an infinite number of stages (86.8%), but can be achieved with a single junction cell. Similarly, the maximum system efficiency calculated for non-concentration with selective emitter as 54 % at T_A = 865 K with the PV cells having bang-gap of 0.92 eV.

In a solar-TPV system, the efficiency increase can be attributed to the minimizing of most of the conversion losses stated in 1.1.2. First, the selective absorber can be designed to absorb a very large percentage of all photons from the sun. Second, the photons emitted directly into the PV cells can have energy close to that of the cell band-gap. Finally, the photon flux from a selective emitter can be much larger than that from the sun because the broad range frequency of sun light is concentrated to a designed wave-length and previously non-useful photons, which had lower energy than the band-gap, were recycled. This larger flux can lead to a larger open circuit voltage.

1.2.2 Benefits of S-TPV Systems

Compared to multi-junction cells, which have a significant limit in terms of how many cells can be stacked together practically, due to materials availability and device design complexity, solar TPV cells shift the complexity to the absorbers and emitters. This shift, in principle, is advantageous because absorbers and emitters are simpler technologically in comparison to multi-junction PV cells. Also, S-TPV energy converters may have weight, size, and cost advantages over other direct energy conversion techniques.

1.2.3 Recent researches on S-TPV systems

In the US, TPV has achieved 22 % efficiency with an emitter at 1200 K [20]. Andreev et al. [21] reported a GaSb cell with an efficiency of 19% when illuminated by a tungsten emitter at 1900-2000 K. Several research directions have been pursued to improve the efficiency and power density in TPV systems: selective emitters based on new materials [22, 23], novel surface structures [24], interference filters [25, 26] based on multilayer thin films and photonic crystals, and photon recycling using a multilayer back reflector [27] placed beneath the photovoltaic cells. Materials for PV cells are based on semiconductors with small band-gaps such as GaSb [28, 29], GaInAs, and GaInAsSb [21]. Radiation tunneling between emitters and PV cell in the near-field

can have significantly higher photon flux than that of the far field [31, 32], and can potentially improve the power density of prototype devices.

1.2.4 Challenges in S-TPV Systems

Solar TPV's efficiency gains come from the spectral control of photons. The spectral control for solar TPV includes two parts. One part of the spectral control is absorption of solar radiation. The other part is the delivery of photons emitted from the solar absorber to the photovoltaic cell.

The later part has been studied more due to the broader application of TPV, other than solar TPVs. Two strategies have been pursued for this photon emission control. One is the control of emission directly by using selective emitters based on new materials [22, 23], novel surface structures [24], interference filters [25, 26], and photonic crystals. The major difficulty with this approach lies in the high temperature operation of the emitters, at which materials can lose their stability. The other strategy is spectral control on the PV cell side, by reflecting back unwanted photons, which are mostly below the band-gap. This approach has the advantage that spectral reflectors on the cell side are operated near room temperature.

So far, many problems associated with selective absorber, selective emitter, and interference filters have been solved. However, no one yet has reported intensive study on thermal stability of selective emitters.

1.3 Thermal Stability of Selective Emitters

From previous research, for high efficiency of S-TPVs, or even for TPV systems, achieving good spectral control at high temperatures is the most challenging part. A detailed explanation of structural spectra control technology, photonic crystals, and the challenges of structural spectra control technology will be given in Chapter 2. However, in brief, the feature size of the spectral control device, in the case of 2-D photonic crystal, is of the order of 100 nm to sub-microns. This nano/micro-scale device cannot maintain its geometrical features and optical performance at very high temperatures, 800 - 1300 ^{o}C, the general operation temperatures of S-TPV and TPV.

Very little research has been reported on the thermal stability of selective emitters. In 2003, Schlemmer reported that recrystallization and surface diffusion to be the major degradation modes of micro-scale selective emitters at 1000 - 1200 °C. But no one has reported physics behind this problem, quantified experimental results of thermal failures or remedies to solve this problem. Therefore, to make the concept S-TPV or TPV commercially successful, thermal stability of selective emitters has been addresses in this research.

1.4 Research Objectives

The objectives of this thesis, accordingly, are to investigate the physics of thermal failures of micro/nano-scale structured selective TPV emitters and to provide a solution for the long term operation of thermophotovoltaic (TPV) power conversion systems. The selective emitter is a periodic micro/nano-scale structure, called photonic crystal, but this small structure loses its structural integrity at high temperature very quickly. Because the TPV system operates at 800 °C to 1300 °C, the feasibility of the entire TPV system is endangered by thermal stability of these selective emitters. In these regards, my research goal is set to provide a solution that can maintain photonic crystal structures at 800 to 1300 °C for more than 10 years (and possibly up to 30 years which is required for practical PV systems in real applications).

1.5. Thesis overview

This section provides a brief overview of the contents, motivation, and key results of the following chapters.

In Chapter 2, through the literature review is introduced the state of the art of the thermophotovoltaics (TPV) systems. The brief history of TPV, its components, operation conditions, along with recent researches for improving conversion efficiency is presented. Current efforts on low-band-gap PV diode development and fabrication and challenges of selective emitters are explained in detail. The challenge of selective emitters' thermal stability and previous studies are summarized.

Chapter 3 identifies the various thermal degradation modes and their physics behind, and the possible solutions. First, grain growth and primary recrystallization issues on polycrystalline

tungsten samples are presented. Pre-annealing minimizes the effect of grain growth on small structures. Second, it was observed that the oxidation of the surface destroyed the entire geometry on top of the surface. A thin layer of diffusion barrier coating could prevent oxidation effectively. In short, 5-7 nm thick sputtered TiN followed by oxygen stuffing could prevent the oxidation to a minimum level. Third, surface diffusion was unavoidable if there were curved structures on the surface at small scale. It has been found that surface diffusion was mostly dependent on the second derivative of the curvature. After long firing tests, it has been found by SEM images and analyzing data that significant evaporation also happens.

In Chapter 4, a novel design concept to prevent or minimize thermal degradation of TPV emitters is presented. For minimizing grain growth and crystallization, pre-annealing the sample prior to micro/nano-scale fabrication or using a single crystalline from the initial step is suggested. For minimizing oxidation and evaporation, surface coatings with a dense film prevent oxygen penetration through and the evaporation of substrate molecule is recommended. The biggest concern was surface diffusion. A flat surface photonic crystal design is proposed to solve this problem. For a 2-D photonic crystal, optically photonic crystal structure, but a physically flat surface is proposed by plugging ceramic materials into each air holes of the photonic crystal surface. By maintaining the flat surface, surface diffusion problem can be basically eliminated. This design, called *Flat Surface Photonic Crystal* (FSPC), is tested with silicon sample at the equivalent thermal condition to tungsten. Since single crystal tungsten based photonic crystal device is expensive to fabricate and difficult to test (high temperature), I have been used a silicon sample, which has well developed fabrication tools and inexpensive processes. Although there are still several issues to solve for using silicon-based flat surface photonic crystals. Several samples have been fabricated for firing and optical performance tests.

In Chapter 5, firing tests for proving the concept and observations after several hours of firing tests are presented. With EDS and SEM images, it has been verified that the geometry was maintained after 100 hours of firing. Silicon-based flat surface photonic crystal did not show any visible inter-diffusion, evaporation, or surface diffusion issues. Furthermore, optical tests followed by firing tests showed the effect of FSPC design on emissivity spectra was negligible. Non-treated samples showed significant loss of emission near IR region, where as silicon-based flat surface photonic crystal maintained its original emission properties.

In Chapter 6, a summary of the research with conclusion and brief statements for the contribution of the research is presented. For future research, several suggestions for improving the design and fabrication of photonic crystal based on Tungsten (W) or Tantalum (Ta) are offered.

Chapter 2

Thermophotovoltaics: State of the Art

2.1 Thermophotovoltaic (TPV) systems

Thermophotovoltaic systems directly convert thermal radiation into electricity. A basic TPV system consists of a thermal emitter and a photovoltaic diode as shown in Figure 2.1. When heated, emitters radiate phonons at various energy levels and photovoltaic diodes capture these phonons and convert some of them into electricity.

When it was first proposed in 1956, the thermophotovoltaic system was similar to solar PV except that the energy source was a low temperature furnace instead of the sun. The system

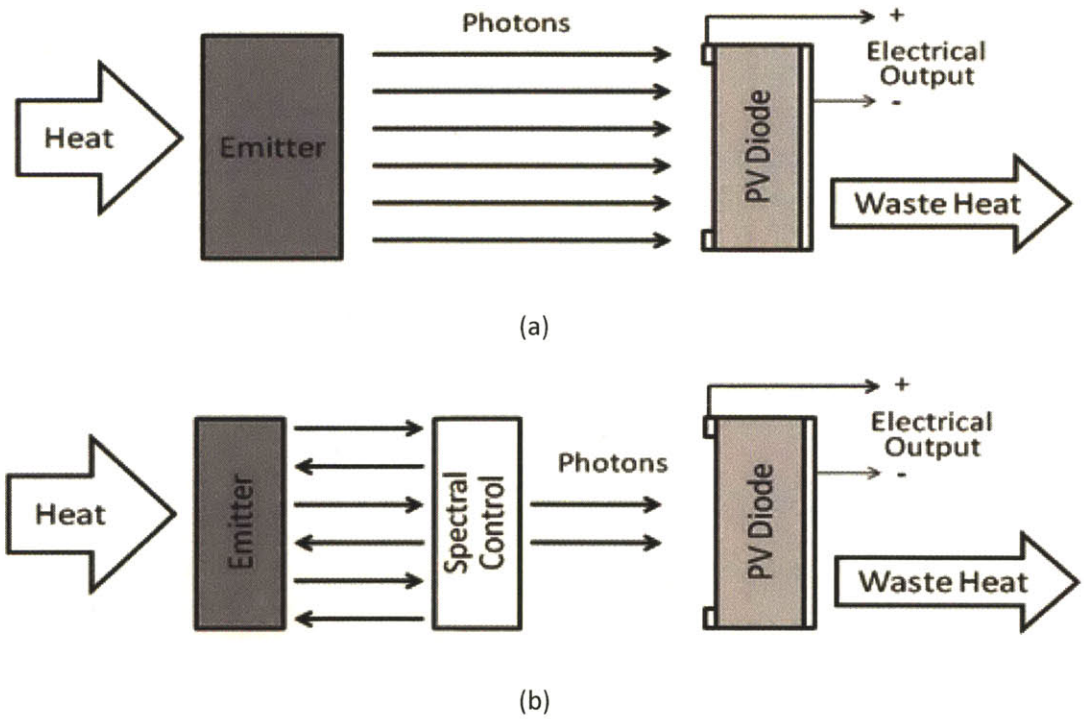

Figure 2.1 Block diagram of (a) an originally proposed thermophotovoltaic (TPV) system and (b) a revised TPV system for improving energy conversion efficiency [14].

could generate electricity at low temperature and consists of simple components with no moving parts.

Previously, thermionic and thermoelectric systems have been limited by the melting temperature of their solid material which also limits the systems' efficiency. However, as opposed to a thermionic or thermoelectric system, TPV isolates photovoltaic cells from the heat source and maintains the cells at room temperature. By creating distance between the emitter and PV cells, TPV avoids conductive heat transfer and allows the collection of energy purely from photons.

The TPV system has been believed to be invented by Dr. Pierre Aigrain who was a visiting professor at MIT in 1960 [33]. It is also known that Aigrain may have gotten the idea from Dr. Henry H. Kolm at MIT Lincoln Laboratory [34]. The oldest recorded document about this idea was written by Kolm in 1956 [35].

Although TPV systems have been studied for several decades, there has been no success yet to bring out a commercially viable product. The system has very low efficiency in the early stages of TPV development during the 1960's, with the highest fuel-to-electricity efficiency at approximately 1-2 % [36, 37]. The huge loss from thermal radiation to photovoltaic energy conversion resulted from the emitters having a very broad wavelength which is largely mismatched with the PV diode's band-gap. In order to achieve higher conversion efficiency, matching the reemitted spectrum to the sensitive spectrum of the PV diode and lowering the photonic band-gap of PV diodes were intensively investigated. However, the limited fabrication technology in the 1960's did not lead to any breakthrough in both controlling the emitter's spectrum and lowering the PV diodes' band-gap.

Along with innovative improvement in micro-fabrication technologies during the 1980's and 1990's, further advances in spectral control designs for both emitters and PV diodes were enabled. Many significant improvements have been reported in both PV diode designs and spectral control designs [38-45].

2.2 Photovoltaic (PV) Diodes

Low band-gap PV diodes are a critical component to achieving high efficiency in TPV systems. The PV diodes convert emitted thermal energy (photons) to electricity. Depending on both the shape of the emitted thermal spectrum and electronic band-gap of semiconductor

material, the efficiency of the TPV system is determined. Each PV diode has a unique band-gap, which is determined by the material's atomic structure as shown in Table 2.1 [46]. An electron or hole may traverse the energy band-gap if provided with energy at least equal to this band-gap energy (E_g). This energy can, for example, be provided by a sufficiently energetic incident photon. From Figure 2.2, the area enclosed by black-body radiation curve and the diode's band-gap represents the useful energy for PV diode input. As the area increases while the band-gap decreases, the TPV system's efficiency will increase. For example, compared with a silicon PV diode, which has E_g of 1.1 eV (corresponding to a wavelength λ_g of 1.1 μm), a GaSb PV diode provides more electricity since its E_g is 0.72 eV.

As seen in Figure 2.2, it is evident that for T < 1800 K, only a small percentage of the radiated photons are absorbed by PV diode, which is the region of wavelengths shorter than 1.1 μm. Therefore, the pairing of a silicon diode and the shown emittance spectra will result in a very inefficient TPV system because the silicon diode only uses a very small portion of the emitted spectrum. Increasing the emitter temperature will shift the peak of radiating spectrum towards shorter wavelengths and will increase the system's efficiency (explained in detail in section 2.4).

However, an increase in emitter temperature will result in serious thermal management problem of the TPV system. Alternatively, PV diode with a lower energy bandgap, which has a longer wavelength λ_g, has been be used. PV diodes can be made from a variety of materials, as seen in Table 2.1. Some PV diodes have very small band-gap energies (such as with quaternary materials like InGaAsSb) and are sensitive to a greater portion of the blackbody spectrum.

Table 2.1 Band-gaps of various TPV materials [46]

Material	Bandgap
Si	1.10 eV = 1.1 μm
GaSb	0.72 eV = 1.7 μm
Ge	0.66 eV = 1.9 μm
InGaAs	0.60 eV = 2.1 μm
InGaAsSb	0.53 eV = 2.3 μm

Although alternative materials lead to higher TPV system efficiency, such diodes' costs are high. Practically, Gallium Antimonide (GaSb, E_g = 0.72 eV, λ_g = 1.77 μm) has been used for PV diodes in TPV systems [48]. Although this material has a larger band-gap than InGaAsSb, it can convert much larger number of incident photons than a Si diode can. Additionally, this material is relatively easy to fabricate using commercial fabrication processes [40].

2.3 Spectral Control

2.3.1 Methods of spectral control

Selective emission may be defined as strong emission at a specific wavelength and weak emission at others. Specifically, selective emitters are considered as a "class of materials whose thermal-radiation emission at equilibrium occurs in a much narrower spectral region compared

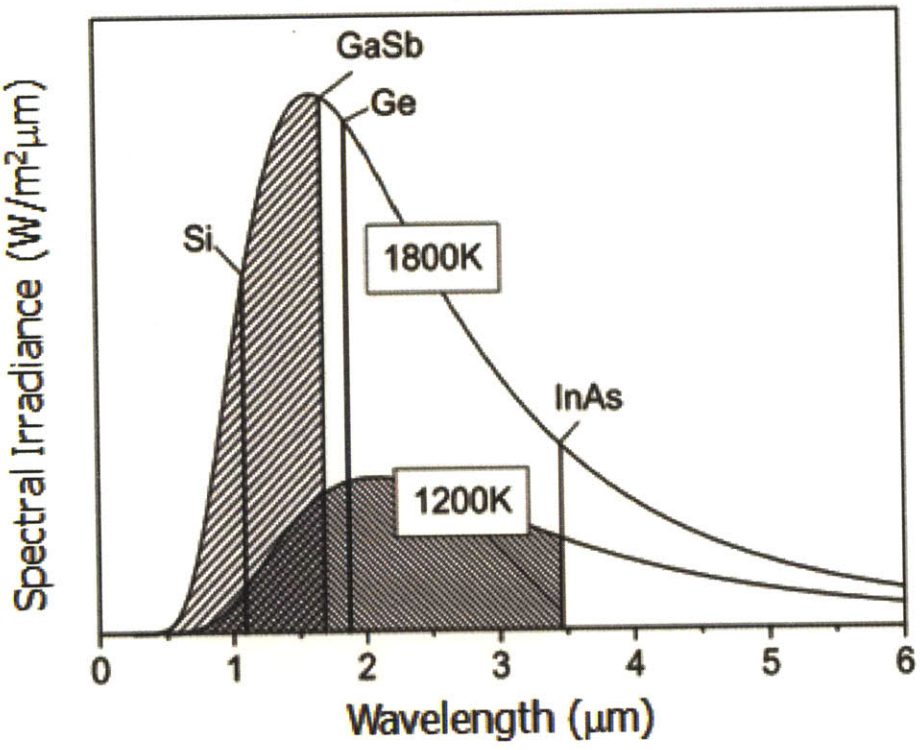

Figure 2.2 Blackbody thermal readiation spectra at 1200 K and 1800 K, band-gaps of some materials are indicated. GaSb and InAs cells photo-response regions are shown by hatched areas of 1800 and 1200 K spectra respectively [16].

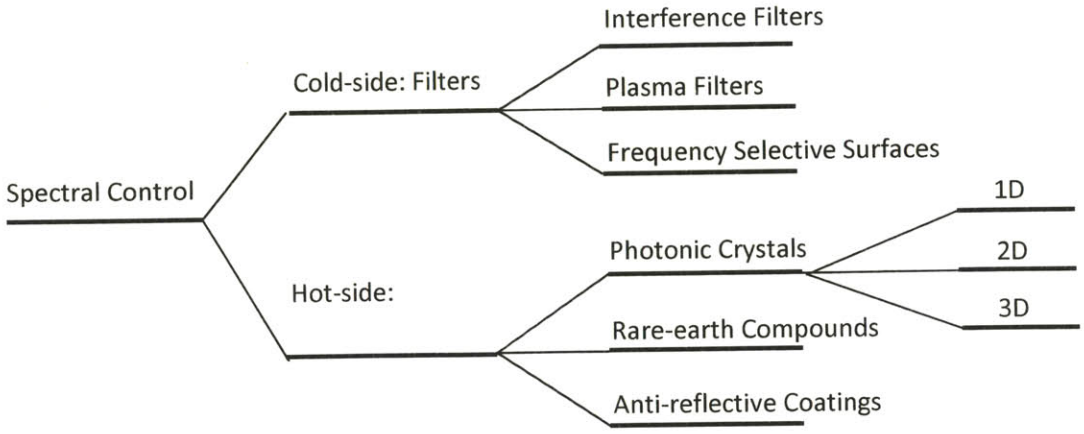

Figure 2.3 Some avenues of TPV spectral control [46].

with that of a black-body at the same temperature" [49]. This selectivity can be achieved by its intrinsic material properties and/or physical structures. Figure 2.3 shows the common approaches to the spectral control for TPV system. Spectral control components can be classified as cold-side and hot-side components. The cold-side components are installed near or on the PV diode. Such cold side components operate near room temperature. The components consist of filters, selective mirrors, and/or anti-reflective coatings on the PV diode. The hot-side spectral control components are attached on or integrated into the emitters. These components, in general, operate at elevated high temperatures of the emitter. These components are termed as selective emitters [46].

First, the rare-earth oxides (holmium or erbium oxide) and transition metals (hafnium or tungsten) show selective emission since their refractive indices changes sharply at the resonant frequency of the material's chemical bonds [50]. These materials with sharply varying refractive indices result in selective emission, which is suitable for TPV. For example, emittance spectra of erbium and ytterbium were found particularly useful since their emittance peaks occur at higher energy levels than the band-gaps of most PV diode materials [43]. The transition metals, such as tungsten and tantalum, also show the variation of refractive index, which can be used for TPV applications with GaSb PV diodes. In short, the refractive index of tungsten provides for increased emittance at wavelengths shorter than 2μm, and suppressed emittance at longer

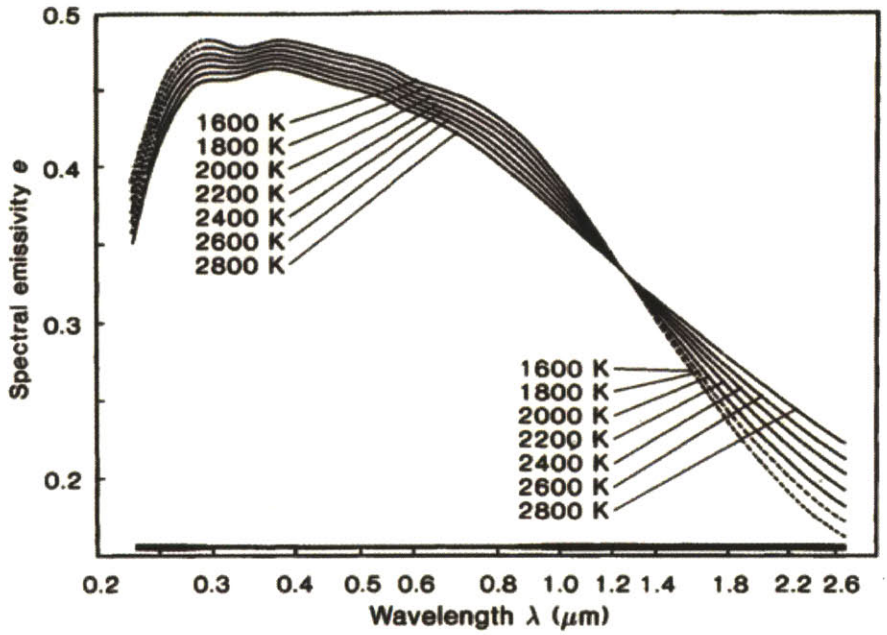

Figure 2.4 Spectral emissivity of tungsten at various temperatures [48].

wavelengths. Its temperature is a big factor, too [48]. Along with its refractive index variation, excellent thermo-mechanical properties (melting temperature of 3422 ^{o}C) of tungsten make it the most common choice of substrate material for TPV emitters.

2.3.2. Photonic crystals

Besides intrinsic material properties, an alternative method for achieving selective emission is by modifying the physical structures of emitter material. These structures are referred to as *photonic crystals* (PhC), which are periodic micro/nano-scale structures that are designed to affect the motion of photons at certain wavelengths. In other words, PhCs are the structures with spatially-periodic variations of the refractive index, where this variation period is on the order of the wavelength of interest [52].

Working principle

Briefly, *photonic crystals* (PhC) comprise periodic dielectric or metallo-dielectric nanostructures that affect the propagation of *electromagnetic waves* (EM) in the same way as the

periodic potential in a semiconductor crystal affects the electron motion by defining allowed and forbidden electronic energy bands. Essentially, photonic crystals contain regularly repeating internal regions of high and low dielectric constant. Since a photon also behaves as a wave, it may or may not propagate through this structure depending on its wavelength. Wavelengths of light that are allowed to travel are known as *modes*, and groups of allowed modes form *bands*. Disallowed bands of wavelengths are called '*photonic band gaps*'. This gives rise to distinct optical phenomena such as inhibition of spontaneous emission, high-reflecting omni-directional mirrors and low-loss-waveguiding [53].

History of photonic crystal as selective emitters

Although photonic crystals have been studied since 1887, the term "photonic crystal" was first used from 1987. In 1987, Eli Yablonovitch and Sajeev John published two milestone papers on photonic crystals [54, 55]. Before that time, only one-dimensional photonic crystals in the form of periodic multi-layers dielectric stacks (such as the Bragg mirror) were studied extensively. Actually, Lord Rayleigh started the` study on one-dimensional (1-D) photonic crystals in 1887 [56]. However, these ideas did not get much interest until 1987.

Yablonovitch's seminal idea was to engineer the photonic density of states, for controlling the spontaneous emission of materials embedded within the photonic crystal emission spectrum control); John's motivation was to use photonic crystals for affecting the localization and control of light (light-guiding). After 1987, the number of research papers dealing with photonic crystals began to increase exponentially. Yablonovitch had demonstrated the first three-dimensional (3-D) photonic band-gap in the microwave regime [57]. The structure that Yablonvitch was able to produce 3-D PhC was a multi-layer-drilled array of holes in a transparent material, which has been called 'Yablonovite', named after him [58].

In 1996, Thomas Krauss first demonstrated a two-dimensional (2-D) photonic crystal at optical wavelengths [59]. This achievement opened up the fabrication methods for 2-D photonic crystals by borrowing the technique of semiconductor fabrication, such as lithography and etching.

Types of photonic crystal as selective emitters

The structuring methods for PhC can be listed as: periodic layers of alternating materials (1-D), posts or holes etched into the surface of the substrate materials (2-D), or three-dimensional volumes with crystalline structure (3-D).

The earliest observation of a 1D PhC was reported by Lord Rayleigh in 1917 [55]. He focused on the reflection of light from skeletal coatings of certain insects. These skeletal coatings are laminar in structure, consisting of a few layers of materials with sharply varying refractive indices. The reflection from such coatings resulted in the observation of different colors depending on the light's incident angle. This publication provided a first insight into the performance of dielectric mirrors. However, this finding was not paid much attention at that time because there were no such techniques by which such a structure could be artificially re-produced. As the evaporation and deposition of thin film developed form semiconductor industry, the 1-D PhCs have found applications, such as selective filters, and perfectly reflective surfaces.

There are two basic types of photonic crystals; those composed of periodic columns and those composed of periodic veins. The behavior of a 2-D PhC depends on many parameters: substrate material, the array kind (square, rectangular, triangular, etc.), and the feature shape (square, oval, round, etc.). The exact characteristics, such as photonic band gap, can be calculated by solving Maxwell's equations. Since the form of the equations can be modified as Eigen value problem for quantum physics, it can be solved by finite-difference, time-domain (FDTD) method.

There are many kinds of 3D PhCs. Diamond arrangements of spheres, face-centered

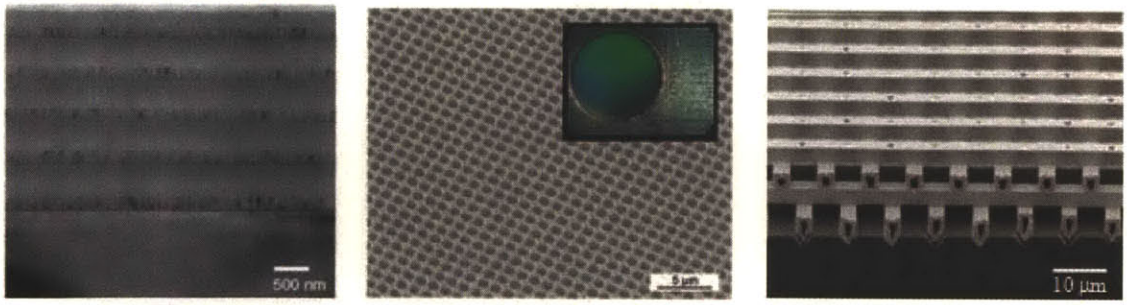

Figure 2.5 Examples of photonic crystals.1D, 2D and 3D [45, 53, 60]

cubic structures, and log-cabin arrangements have been investigated in view of the fabrication technique developments in recent years. Although significant developments have been made in the fabrication of these structures, the fabrication processes are still quite complex.

Fabrication challenges of photonic crystals

With the rapid development of micro/nano-fabrication techniques, researchers have focused on manufacture of highly-efficient selective emitters, Figure 2.4. However, the study of three-dimensional photonic crystals has proceeded more slowly than their two-dimensional counterparts. This is because of the increased difficulty in fabrication.

Although there was no inheritance of readily applicable techniques for fabricators of 3-D photonic crystals, some attempts have been made: "woodpile" structures and "self-assembly of nano-spheres." However, these techniques for 3D fabrication are significantly more complicated, time-consuming and expensive [57-60].

Therefore, although the 3D PhCs offer the most efficient selective emission performance among PhCs, recent researches are more focused on developing 2-D PhCs with transition metals [55, 56].

2.4 System Efficiency of TPV

In Chapter 1, it was mentioned that the maximum theoretical system efficiency for infinite-junctions photovoltaic is 86.8% and that of ideal S-TPV is 85.4%. In practice the reported maximum efficiency for multi-junction photovoltaic system is 40% and that of S-TPV is about 22%. However, researchers anticipate the maximum system efficiency of up to 60% can be achieved in both cases.

A TPV system's efficiency can be determined as the product of three major conversion efficiencies: emitter efficiency, spectral efficiency and PV diode efficiency. Emitter efficiency (η_E) is defined as the ratio of the radiated energy to the chemical (or any) energy used to heat the emitter. Spectral efficiency (η_{SC}) is the amount of energy below the band-gap wavelength with respect to the total energy radiated by the emitter across the entire wavelength spectrum. PV

diode efficiency (η_{PV}) is defined as the ratio of the electrical energy output to the photon energy incident upon the diode, see Equations (2.1) - (2.4).

$$\eta_{sys} = \eta_E \times \eta_{SC} \times \eta_{PV} \tag{2.1}$$

$$\eta_E = \frac{Net\ radiation\ power\ from\ emitter}{Chemical\ energy\ input\ flow} \tag{2.2}$$

$$\eta_{SC} = \frac{Radaition\ power\ absorbed\ by\ PV\ diode}{Net\ radiation\ power\ from\ emitter} \tag{2.3}$$

$$\eta_{PV} = \frac{Electrical\ power\ output}{Radaition\ power\ absorbed\ by\ PV\ diode} \tag{2.4}$$

In most cases, the emitter efficiency and the PV diode efficiency are almost fixed by heat sources and PV material selection. Therefore, to achieve high system efficiency, high spectral control efficiency is required.

There are two key parameters that determine spectral control efficiency: emitter temperature and selective emitter performance. If the emitter is assumed to be blackbody, the spectral control efficiency can be redefined as the ratio of the area under the blackbody radiation curve in the entire range of wavelength (entire radiation energy from emitter) to the area under that blackbody radiation curve below PV diode band-gap (the hatched area in Figure 2.2, which is convertible radiation with PV diode). As the emitter temperature increases, the peak wavelength moves to the shorter wavelength; thus, this area (or percentage) of convertible radiation increases, see Figure 2.2.

There are many researches reporting on TPV system efficiency. Based on their fabricated 3D PhCs with GaSb photovoltaic cell of operating temperature at 1800 K, Gee and his colleagues reported the calculated maximum system efficiency as 26.9 % [61]. Previously, Henry calculated the overall TPV system efficiency with 1D tungsten PhCs with silicon PV diode at operation temperature of 1200 K as 21.7 % (the view factor was 1.0) [62]. Most recently, Bernal and his colleagues calculated their maximum micro-TPV system efficiency with 2D tungsten emitter with GaSb PV diode as 26.2 % (the view factor of 0.4) [63]. However, these

are the calculated numbers based on assumption and modeling. Depending on the combination of spectral control device and PV diode, and emitter temperature, the TPV's theoretical system efficiency varies considerably. The prototypes of micro-TPV power generator achieve a fuel-to-electricity conversion efficiency of about 3%. Although it is not high but it is three times greater than that of a lithium ion battery of the same size and weight. It's been achieved with butane fuel, tungsten selective emitter, and 1-D filters [61].

2.5 Thermal Stability Issues

The general TPV's emitter temperature is 800 -1300 °C. As it can be seen in Figure 2.2, higher emission temperature promises higher system efficiency. However, the maximum temperature of emitter is limited by its material properties. Silicon carbide (SiC) is known to be stable up to 1700 °C, but it has very high emission spectrum on long wavelength regime. The most common material used for TPV emitter is tungsten. Tungsten itself has selective emission properties, with micro/nano patterned PhCs structure promising good spectral control. However, even though it has a high melting temperature at 3422 °C, tungsten starts to oxidize at 750 °C [62].

There are a few studies reporting the thermal stability issue of tungsten PhCs. Schlemmer and his colleagues conducted thermal tests on tungsten PhCs and pointed out the modes of thermal degradation: recrystallization, surface diffusion, and oxidation [63]. However, more research on degradation modes and practical solutions for them are required for real-world application of TPV systems.

Chapter 3

Thermal Stability and Failure Modes of Selective Emitters

3. Identification of Thermal Failure modes of TPV emitters

Nano or microstructures on selective emitters will be degraded or disappear when they experience high temperatures over certain duration of time. Considering that a TPV is expected to be operatable over 10s of years, it is the biggest challenge whether the nano/micro patterned emitters would survive the temperature during that time. Identification of failure modes was the highest priority task to seek solutions for preventing thermal degradation of micro/nano structures. We performed firing tests and observed the results with polycrystalline tungsten sample at 1200 °C. The major degradation modes found were grain growth, oxidation, surface diffusion and evaporation. Some of the degradation modes were also confirmed with silicon samples at 400 °C (T_h = 0.4). Although each mode is possibly coupled with others, we tried to seek independent solutions to prevent the thermal degradation problem fundamentally by observing and studying the physics behind the thermal degradation.

3.1. Recrystallization and Grain Growth

3.1.1 Recovery, recrystallization and grain growth

When strain hardened materials are exposed to elevated temperatures, three things can occur during the subsequent heat treatment: recovery, recrystallization, and grain growth.

First, when stain-hardened material is held at an elevated temperature an increase in atomic diffusion occurs that relieves some of the internal strain energy. Because atoms are not fixed in position but can move around when they have enough energy to break their bonds, the excited energy allows atoms in severely strained regions to move to unstrained positions. This is

known as *recovery*, in which only internal residual stresses are lowered due to the reduction in the dislocation density and a movement of dislocations to lower-energy positions. This process happens in areas called sub-grains. Since there is no grain migration or nucleation, there is no appreciable reduction in the strength and hardness of the material. Sometimes it improves corrosion resistance.

At a higher temperature, new, strain-free grains nucleate and grow inside the old distorted grains and at the grain boundaries. These new grains grow to replace the deformed grains produced by the strain hardening. This is called *recrystallization*. It depends on the temperature, the amount of time at this temperature and also the amount of strain hardening that the material had experienced. The more strain hardening, the lower the temperature will be at which recrystallization occurs. A minimum amount of cold work is necessary for any amount of recrystallization to occur. The size of the new grains is also partially dependent on the amount of strain hardening. The greater the stain hardening, the more nuclei for the new grains, and the resulting grain size will be smaller.

If a specimen is left at the high temperature beyond the time needed for complete recrystallization, the grains begin to grow in size. *Grain growth* occurs when recovery and recrystallisation are complete and further reduction in the internal energy can only be achieved by reducing the total area of grain boundary.

For 2-D photonic crystals, the micro/nano-scale structure is much bigger than the size of atoms but smaller or similar order with the grain size. If the fabricated arrays of 2-D photonic crystal experience the recrystallization or grain growth, the physical geometry of the micro/nano features could be altered by moving the boundaries of each micro/nano-hole resulting in different/inferior optical performance as selective emitters.

3.1.2 Recrystallization of tungsten

In most cases, poly-crystalline tungsten sheet is produced by work hardening process, rolling process. Although the sample is strain-free, recrystallization and grain growth still can occur. The pure tungsten has a very high recrystallization temperature, of approximately 1350 °C. However, its recovery starts at around 300 °C. Sometimes, even before recrystallization, grain growth can start without recrystallization. That means, the photonic crystal structure of a poly-

crystalline substrate can deform or migrate at the general operation temperature of themophotovoltiacs, 800 °C - 1300 °C.

3.1.3 Suggested solution for poly-crystalline tungsten

Pre-annealing, which makes the sample experience recovery, recrystallization, and grain growth, the tungsten before fabricating micro/nano-scale structure may result in minimizing the deformation by grain growth or recrystallization [73]. Also, already grown grains by annealing slows its speed of grain growth when it reaches a certain point, order of hundreds of micron, there is little effect of grain growth for the annealed samples. Some micro/nano-scale structures on the grain boundary may be deformed by the grain boundary migration, but if the grain size reached a large enough size, the portion of the holes sitting on the grain boundary is small enough to ignore. Alternative solution will be just using single crystalline tungsten since there would be neither recrystallization nor grain growth issues.

3.1.4 Preliminary test with poly-crystalline tungsten

Preliminary firing experiments have been conducted to observe grain growth of a polycrystalline tungsten sample. 10 mm x 10 mm polycrystalline tungsten samples were prepared by mechanical polishing. Surface roughness was less than 0.5 μm and its thickness was 300 μm. First, 20 holes (array of 4 by 5) of 5 μm-diameter were drilled using focused ion-beam milling process,

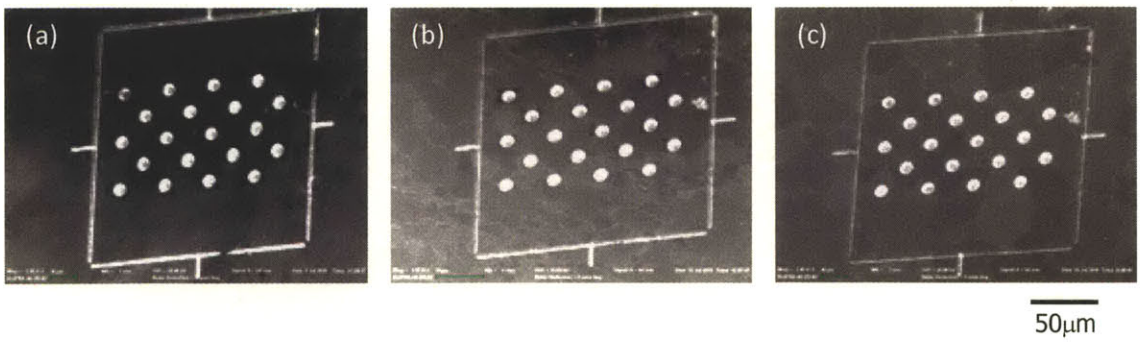

Figure 3.1: Thermal stability test of micro holes on poly-crystalline tungsten surface: (a) polished surface with focused ion-milled 5μm diameter and 2μm deep trenches, (b) 50-hour annealing at 1,200 °C, and (c) 100-hour annealing at 1,200 °C (Grain growth has been observed, SEM images are 30-degree titled view. Fabrication details are in Appendix B.1)

Appendix B. Spacing between the holes was 20 μm and the depth was 5μm as shown in Figure 3.1. The sample was fired in an oxygen free condition at 1200 °C for 100 hours.

The samples were observed in an on SEM at 50 and 100 hours of firing. The temperature was gradually increased to 1200 °C at a rate of 3°C/min and stayed for 50 hours. To remove possible oxygen molecules on the surface, the forming gas, hydrogen (5%) and nitrogen (95%) was allowed to flow at 150 sccm. The hot sample was cooled down to room temperature at a rate of 3°C/min under same forming gas flow. A set of SEM images after 50 hours of firing were obtained. The same procedure was repeated for additional 50 hours to obtain 100 hours of firing results as shown in Figure 3.2. A closer look at the micro holes reveals the recrystallization (and/or grain growth) along with the surface diffusion (see Figure 3.2).

3.1.5. Pre-annealing

Using single crystal material will free the samples from the grain growth issue. However, by pre-annealing the samples prior to micro/nano fabrication on the surface, we could also minimize the effect of grain growth. Since primary-recrystallization and grain growth occur

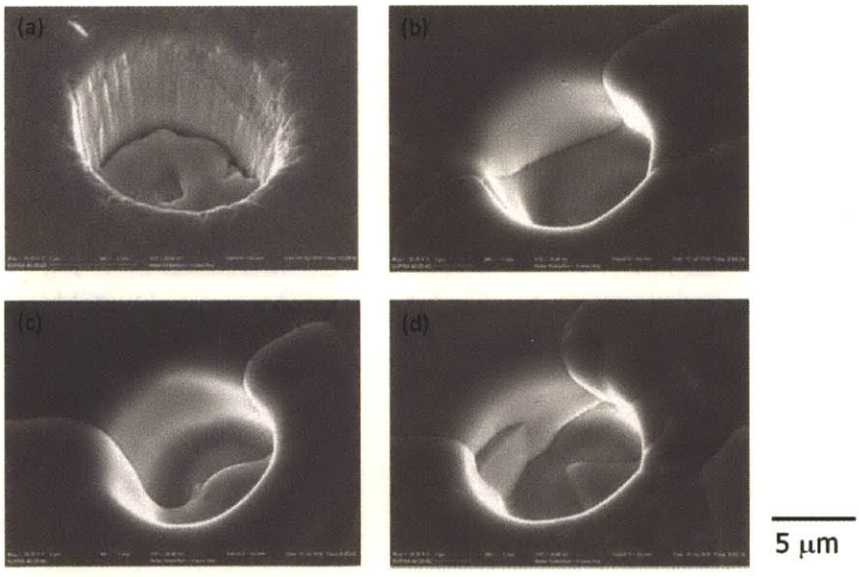

Figure 3.2: Thermal stability test of micro holes on poly-crystalline tungsten surface: (a) polished surface with focused ion-milled 5 μm diameter and 2μm deep trenches; (b), (c) and (d) 100-hour annealing at 1,200 °C (Grain growth and surface diffusion are observed. Fabrication details are in Appendix B.1)

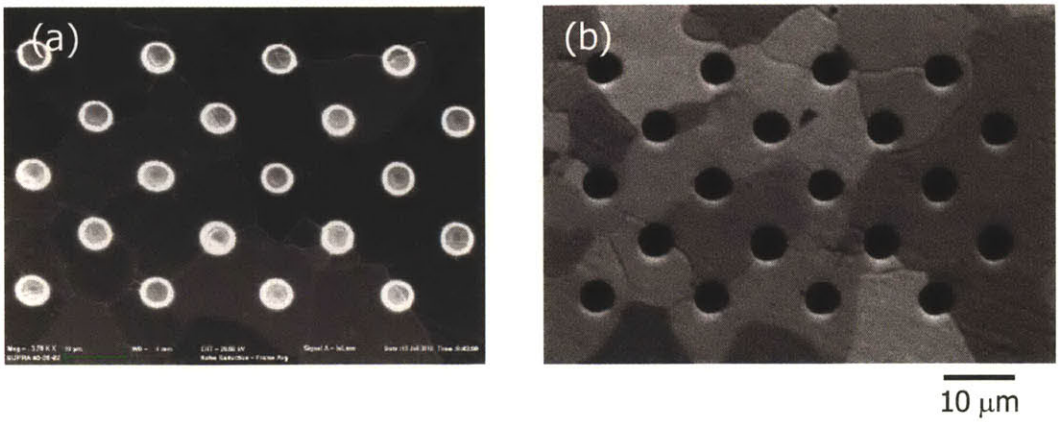

Figure 3.3 (a) 100-hour annealed at 1200 °C and (b) additional 40-hour annealing at 1200°C. Polished poly-crystalline tungsten, twenty holes were drilled using focused ion beam milling and fired for 100 hours. Fast grain growth was observed in the beginning (Figure 3.1), but once fired at 1200 °C for 100 hours, additional firing for 40 hours did not show much increase in grain size.

when the material has stored energy due to deformation, preannealing would relax these stresses and can recrystallize small grains to a certain level of stable size and minimize the effect of grain growth.

The grain structure was observed after 100 hours pre-annealing at 1200°C and additional 40 hours annealing at 1,200°C as shown in Figure 3.3. The grain boundaries did not move significantly, i.e., the grain size did not change much during the additional 40 hours.

To see the effect of pre-annealing, two polycrystalline tungsten samples were tested. One is polished, pre-annealed and then drilled with holes using focused ion beam milling (FIB). The other is just drilled with holes using FIB without any other treatment except polishing the surface. Pre-annealing condition was 1,200 °C for 100 hours with ramping up and ramping down at 3°C/min. The samples were put together into the furnace with hydrogen (5%) and nitrogen (95%) flowing condition to prevent oxidation. After firing at 1200 °C for 100 hours, it can be noted that pre-annealing effectively prevents the degradation by grain growth. As it can be seen in Figure 3.4, (a) and (e) are pre-annealed samples and (b) and (f) is non-treated samples. These four samples fired at 100 hours at 1200 °C and (c), (d), (g), and (h) are the corresponding SEM images. It was clear that pre-annealed samples survived longer than non-treated samples from the grain growth and/or surface diffusion.

3.2. Thermal Oxidation

Tungsten samples were fired in various low-oxygen partial pressures and X-ray diffraction was used to track the presence of Tungsten trioxide (WO_3). It was found that even at a controlled condition with forming gas supply, the surface chemistry was changed (oxidized). So the idea of coating the surface with a diffusion barrier material has been tested.

3.2.2. Oxidation

Oxidation may impact the geometry of micro/nano-scale structures on the surfaces, and in the case of selective emitters, any chemical change can significantly alter the emitted spectrum as well. For example, in air, tungsten begins to oxidize at room temperature with significant oxidation occurring around 400-500 °C. Tungsten trioxide (WO_3) is permeable to oxygen which allows the oxide layer to grow quickly. If tungsten is heated, further sublimation will begin around 750 °C. It is, therefore, critical to understand the exact relationship between the oxidation rate, the partial pressure of oxygen, and the temperature [74]. It is estimated that even at a very low partial pressure of oxygen of 10^{-12} Torr and a temperature of 1,100 °C, the surface will

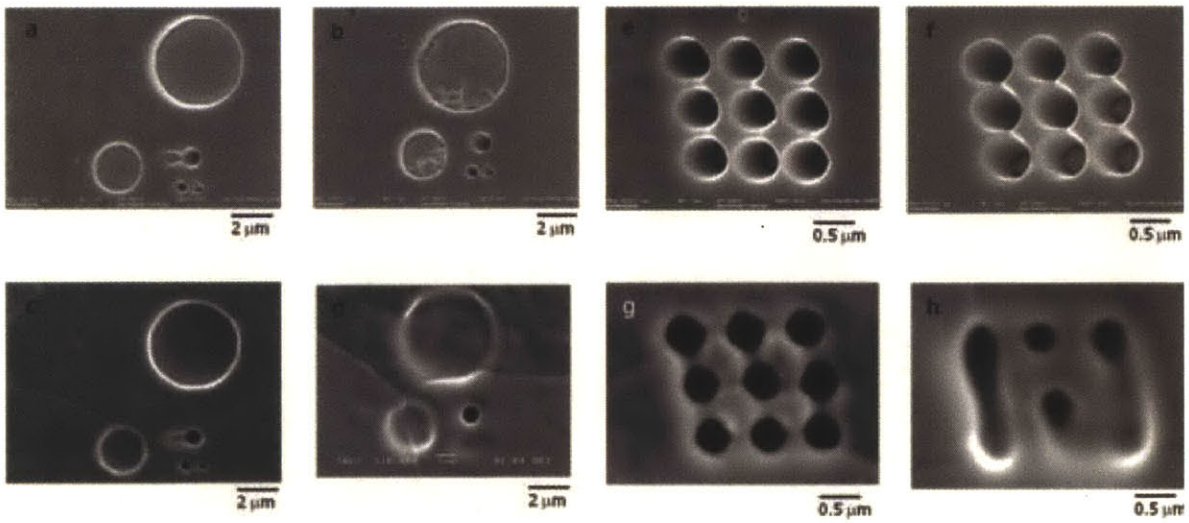

Figure 3.4 (a) Pre-annealed for 100 hours at 1200 °C before drilling the holes, (b) non-treated polished tungsten with drilled holes, (c) and (d) 100-hour firing at 1200 °C in almost oxygen free condition. (e) and (f) were treated by the same method as (a) and (d) but with nano-scale holes, diameter of 300 nm, (g) and (f) are images after 100 hours firing at 1200 °C. Details of fabrication process are in Appendix B.1.

oxidize at a rate of approximately 8 nm/day (Equation (3. 1)):

$$-\frac{dM}{dt} = 256 \cdot P_{O_2} \cdot e^{-\left(\frac{25,400}{RT}\right)} \tag{3. 1}$$

where *dM/dt* is the mass lost to oxidation per unit time in g/cm^2/min, *T* is the absolute temperature in Kelvin, and P_{O2} is the oxygen partial pressure in Torr. This highlights the challenge presented for preventing oxidation, as well as the importance of a good diffusion barrier coating. A single crystalline tungsten sample is prepared, which is free from grain growth and/or recrystallization, was polished and drilled with various shapes and sizes of holes and trenches. To deliver harsh condition on oxidation, rather than hydrogen and nitrogen flow, I allowed only nitrogen flow for oxidation test. After firing for 30 hours at 1200 °C in nitrogen at 5 sccm flowing condition, the oxidation on the tungsten surface could be observed. In Figure 3.5, (a), (b), and (c) are the various size and shapes of trenches, after firing these at 1200 °C for 20

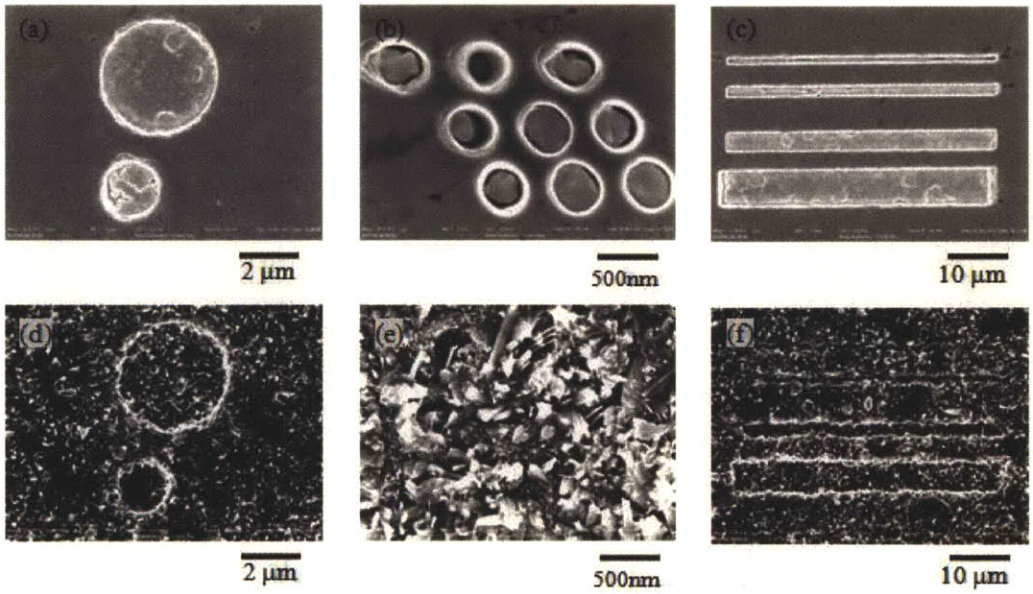

Figure 3.5 Oxidation on the tungsten surface after 20 hours of firing at 1200 °C. Nitrogen flow was at 5 sccm. (a) is top view of SEM image of 5 μm and 2 μm holes, (b) is 300 nm holes and (c) is the 50 μm-long 500 nm, 1 μm, 2 μm and 5 μm width trenches; (d), (e) and (f) are 20 hours later for each sample from (a), (b) and (c) respectively.

hours, significant degradation of the surface by oxidation is found. The oxidation is verified with XRD analysis. In Figure 3.6, the tungsten trioxide peaks appeared after 20 hours firing at 1200 °C, which was not detected previously at 10-hour firing.

3.2.3. Diffusion barrier coating

For high temperature diffusion barrier, titanium nitride (TiN), tantalum nitride (TaN), Aluminum oxide (Al_2O_3), hafnium oxide (HfO_2), and silicon carbide (SiC) are the common materials to be coated on the metal surface [75, 76]. However, the oxides have relatively weak adhesion on metal surface and SiC has relatively low melting temperature compared to TiN or TaN. TiN was chosen since it has a smaller thermal expansion coefficient compared to W. (A more detailed discussion about material choice is given in Chapter 4.) It is also reported that oxygen stuffing on sputtered TiN can enhance the diffusion barrier quality since sputtered TiN has columnar structure and oxygen can fill the gap between the grains by stuffing method [77].

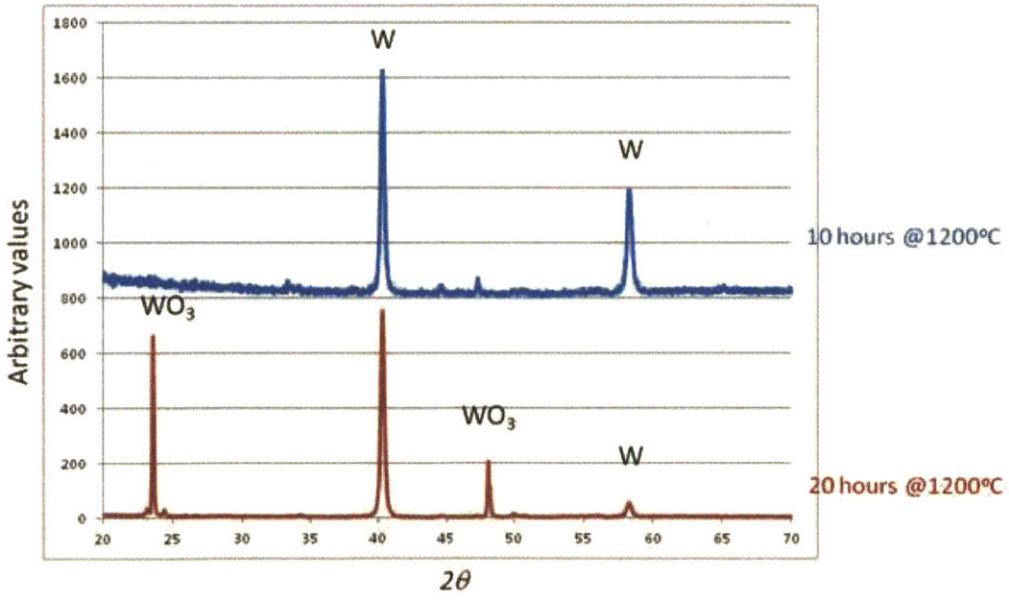

Figure 3.6 XRD data were taken after firing at 1200 °C for 10 and 20 hours. But, the peaks of Tungsten trioxide (WO_3) are very weak after 10 hours of firing at 1200 °C, which could be observed after 20 hours of firing at same temperature.

3.2.4 Test with TiN coating

TiN layer, coated by sputtering, can be a solution for preventing oxidation. To have dense diffusion barrier, the samples were TiN coated by sputtering at 400 °C and then heated at 300 °C for 30 min in air for stuffing oxygen.

Through the firing tests, it was found that 5-7 nm-thick coating of TiN was effective. Three different samples were prepared: (a) TiN coated, (b) TiN coated with oxygen stuffing, and (c) exposed tungsten samples without any coating. These samples were fired at 1200 °C for 30 hours, and after every 10 hours, SEM images were obtained for each sample. As seen in Figure 3.7 and 3.8, TiN coated samples, (b) and (c), survived but the samples without the TiN barrier, (a), were completely destroyed.

3.3. Surface Diffusion

Thermally driven diffusion of atoms constantly occurs in all materials. While it tends to be negligible in solids at low temperatures, as the temperature increases the rate at which diffusion occurs begins to dominate the evolution of the material geometry. In the case of micro/nano-scale structures, surface diffusion tends to dominate bulk diffusion. Surface diffusion may be thought of as random thermal motion of atoms on a surface. However, because the amount of surface atoms varies based on the geometry of the structure, some areas of a surface may experience more diffusion than others and a net material flow occurs.

3.3.1 Mullin's Equation

To investigate surface diffusion further, a theoretical modeling of thermal degradation of the micro/nano-scale structures is proposed. Based on Mullin's analysis, Equation (3.2), the second derivative of the curvature along the surface, the coefficient of surface diffusion, the interfacial free energy are the key parameters that affect the spatial distribution of surface diffusion [78].

Based on Mullin's equation, the degradation of the 2-D trench by surface diffusion is simulated. For single crystal tungsten, a significant change on the radius of curvature started after 10 hours at 1200 °C and the flatness of the bottom of the hole clearly altered after 50 hours at 1200 °C.

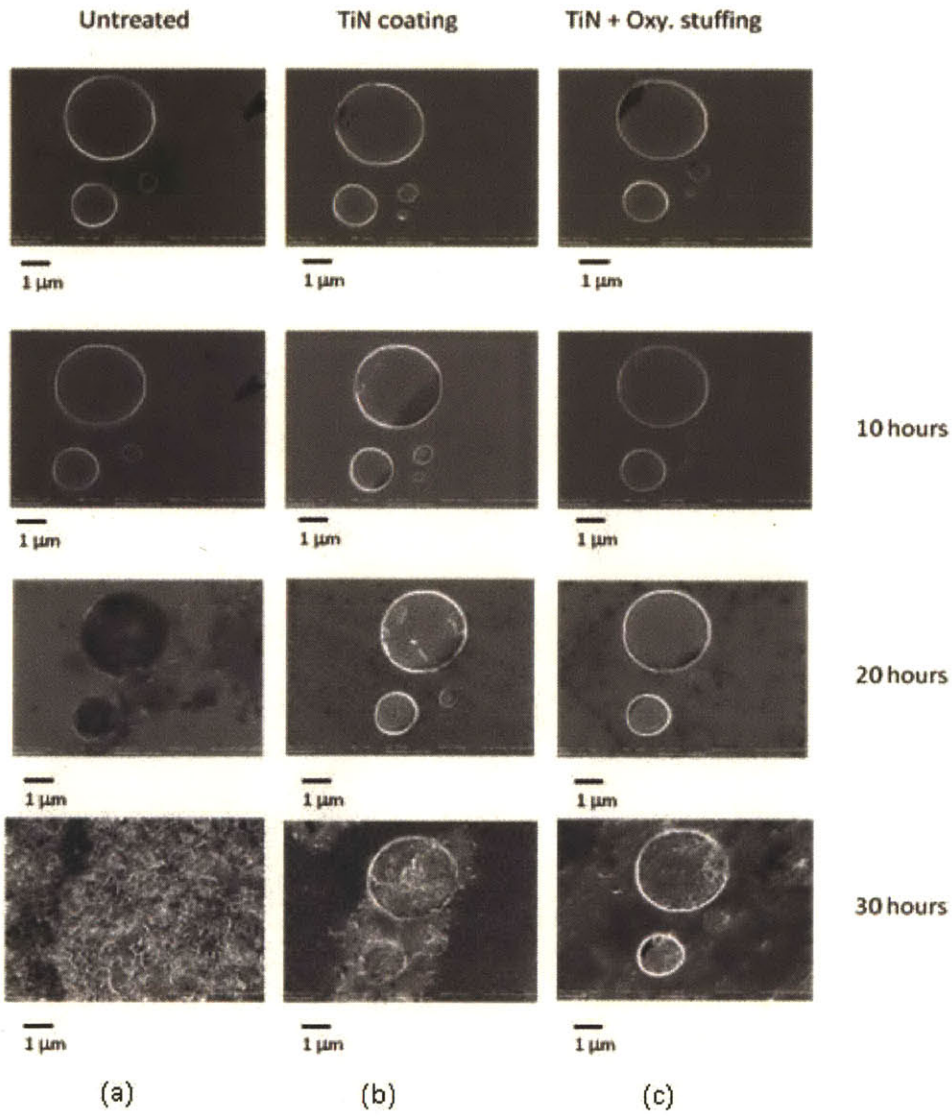

Figure 3.7 Oxidation of tungsten surface. (a) untreated sample, (b) TiN coated and (c) TiN coated and oxygen stuffed. Images captured every 10 hours after firing at 1200 °C. Total 30-hour firing test results under nitrogen flowing at 5 sccm. Ramped up and down at a rate of 3 °C/min.

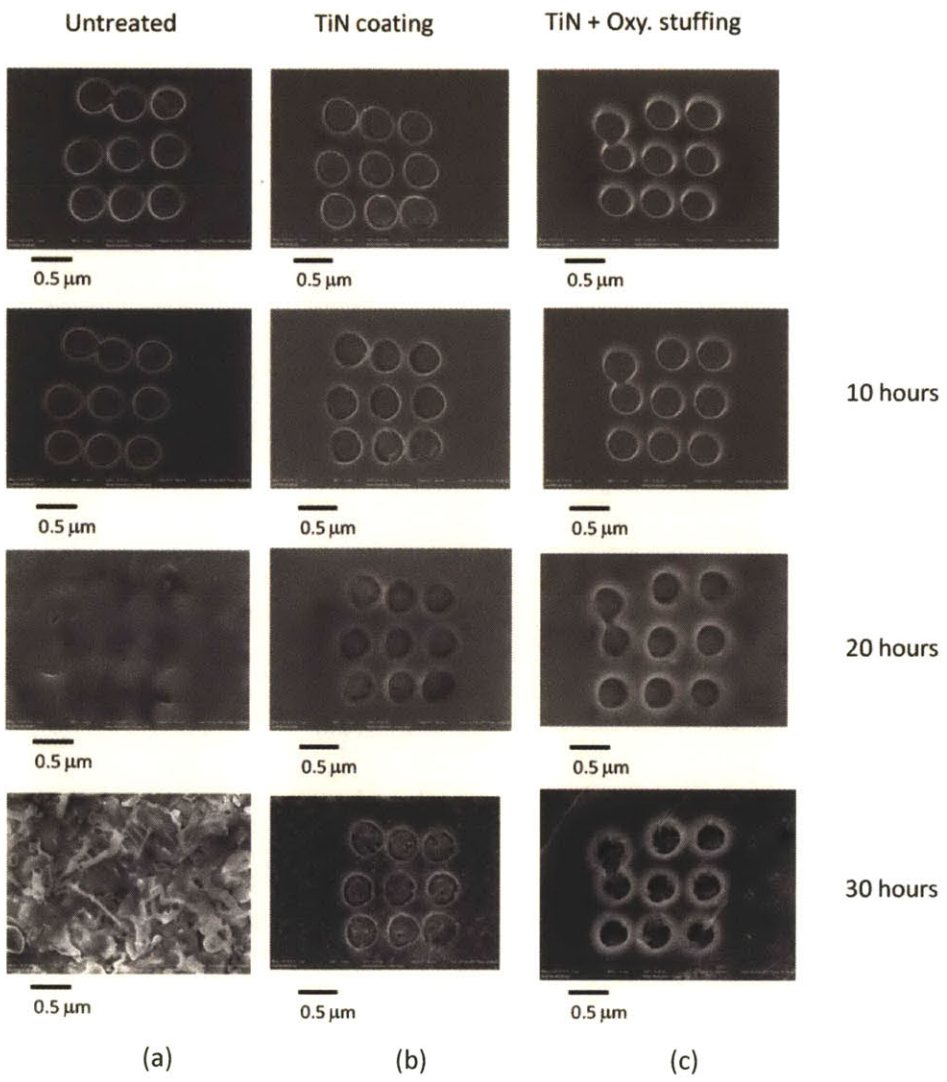

Figure 3.8 Oxidation of tungsten surface. (a) untreated sample, (b) TiN coated and (c) TiN coated and oxygen stuffed. Images captured every 10 hours after firing at 1200 °C, same test sample but nano-scale structures. Total 30-hour firing test results under nitrogen flowing at 5 sccm. Ramped up and down at a rate of 3 °C/min.

However, for given operation conditions, generally isothermal and isobaric, surface diffusion is fully determined by the second derivative of curvature. This is because all the other parameters are identical for the same temperature, pressure and material. The velocity of the surface in the normal direction, v_n, is then given by:

$$v_n = \gamma \Omega^2 n \frac{D_s}{kT} \frac{\partial^2 K}{\partial s^2} \tag{3.2}$$

where γ is the interfacial free energy, Ω is the atomic volume, and n is the number of atoms per unit area. D_s is the coefficient of surface diffusion, k is Boltzmann constant, T is absolute temperature, and $\partial^2 K/\partial s^2$ is the second derivative of the curvature of the surface.

3.3.2. Modeling and simulation

Although some of the parameters are adopted from other research such as the surface diffusion coefficient and the surface interfacial energy [79], this calculation is mainly dependent on both partial press of forming gas and the firing temperature.

For the 3-D simulation of cylindrical tungsten holes, we used a method called the level-set method. A finite element solver (COMSOL) is used to monitor the evolution of the surface with respect to time at 1200 ^oC (T_h = 0.4) (Figure 3.9 - 3.11, Appendix A).

From both the 2-D and 3-D modeling and simulations, there was not much change in the width of trenches during the first 50-100 hours but the curvature at the corners changed significantly. To link the geometric deformation to the emissivity spectra, Maxwell's equations for transmission and reflection spectra over a wide spectrum of frequencies need to be solved. We used the Meep (or MEEP), which is a free finite-difference time-domain (FDTD) simulation software package developed at MIT [80], to model electromagnetic systems and calculate emission spectra with deformed 3-D geometry.

By modifying general MEEP code for emission spectra calculation with specific 3-D geometry input, we could obtain the emission spectrum of these degraded samples with respect to time at 1200 ^oC, see Figure 3.11. As seen in Figure 3.11, the area enclosed under power spectrum decreases with time. It means that the emitter radiates less photons at lower wave

length and radiated more at the longer wavelength region, which results in decreased emission power.

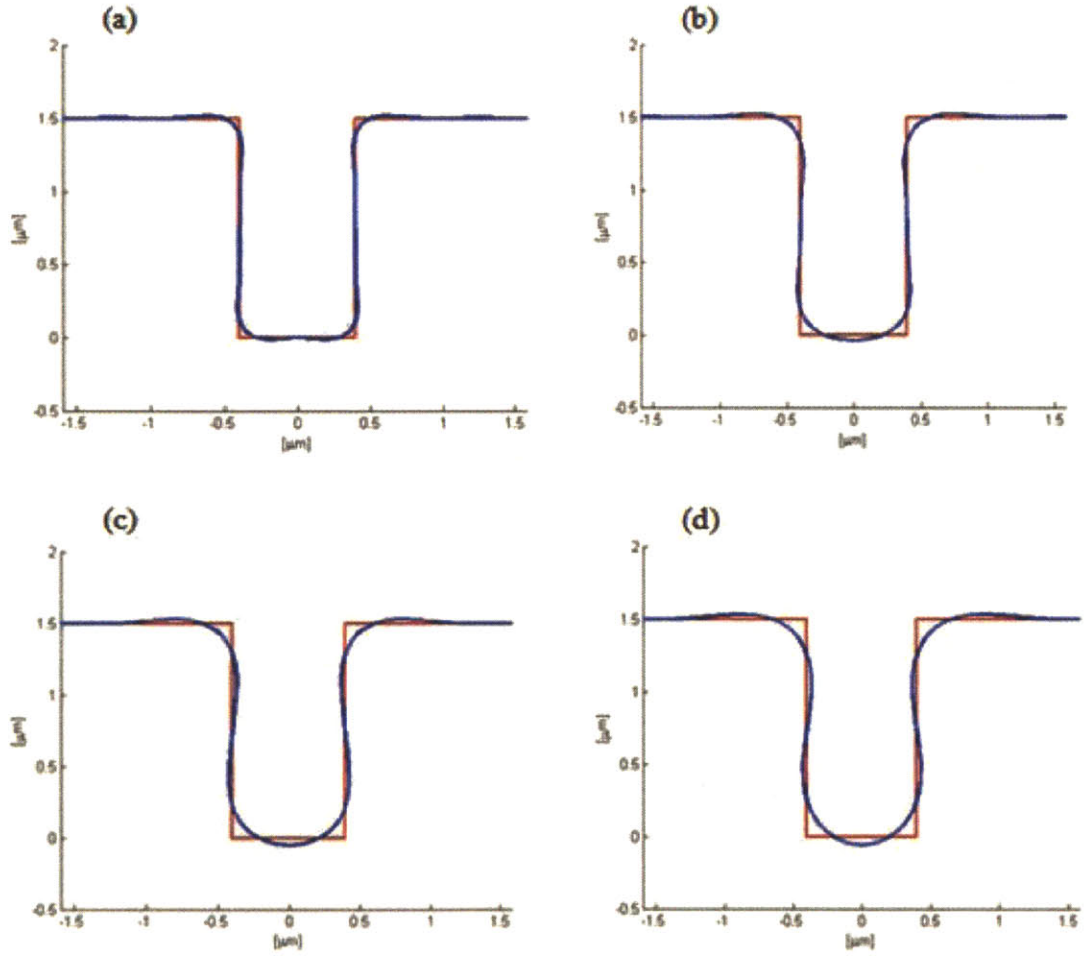

Figure 3.9 2-D modeling of tungsten surface diffusion at 1200 °C (T_h = 0.4), 1.5 μm depth and 1 μm width: (a) 10 hours, (b) 50 hours, (c) 100 hours, and (d) 200 hours.

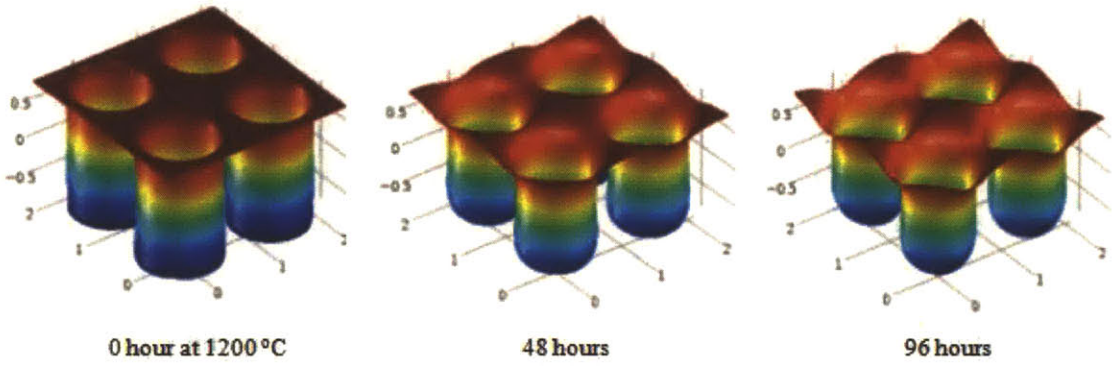

Figure 3.10 3-D modeling for 1200 °C ($T_h = 0.4$), (with Michael Ghebrebrhan in collaboration, 1μm diameter, 2μm depth and 1.6 μm period.

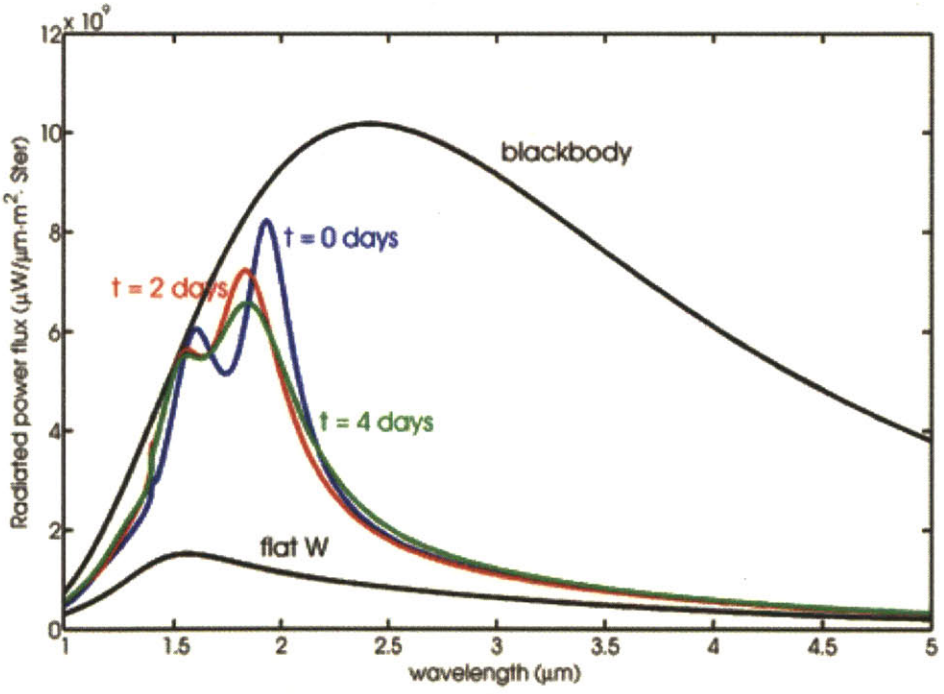

Figure 3.11 Calculated radiative flux at 1200 °C form the degraded sample by surface diffusion at 1200 °C. The simulation is done with Michael Ghebrebrhan by using MEEP, Appendix A.

3.3.3 Experiments for surface diffusion

Single crystalline tungsten and silicon samples were prepared for firing tests. To avoid coupled effects of grain growth or recrystallization, single crystalline materials were chosen. To minimize oxidation, in addition to nitrogen, hydrogen (5%, 20 sccm) was flown during the entire time of the firing tests. For observation of surface diffusion on single crystalline tungsten and silicon, prepared samples were not coated with a diffusion barrier.

Tungsten micro/nano-holes were fabricated using focused ion beam milling (details of fabrication parameters for focused-ion beam milling are in Appendix B.1). Silicon micro-trenches and nano-holes were fabricated using interference lithography and dry etching techniques, see Figure 3.12 and Figure 3.13.

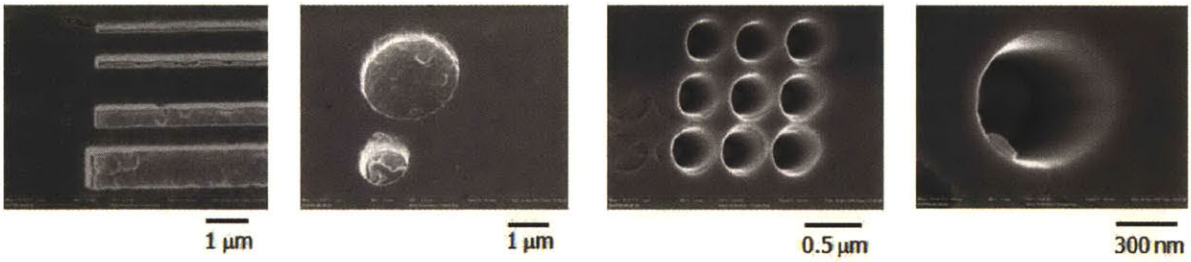

Figure 3.12 Fabricated single crystal tungsten by focused-ion beam milling (FIB), 30-degree tilted views.

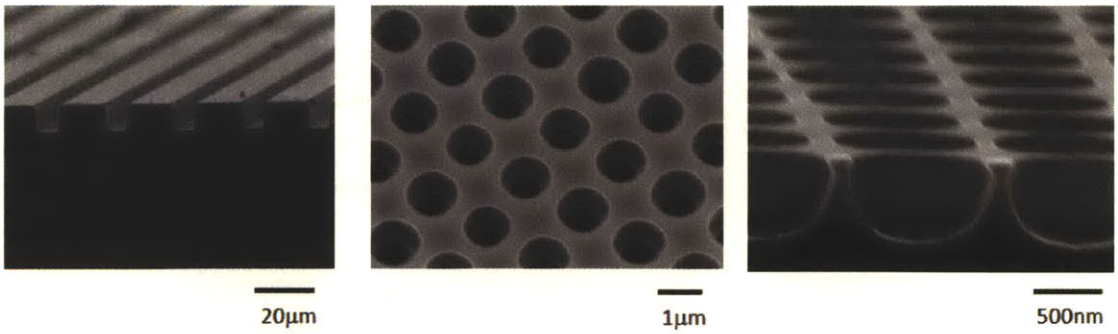

Figure 3.13 Fabricated single crystalline silicon by interference lithography and Deep RIE method: (a) micro-trench (2 degree tilted), (b) 1 μm diameter array of holes (30-degree tilted), and (c) cross-sectional view of sample (b) (2-degree tilt, details of fabrication process and parameters are in appendix B.2).

Unfortunately, firing tests with tungsten sample had several issues: fabrication, cross sectional observation, and firing test setup (a detailed explanation and suggestions will follow in Chapter 6). In this reason, silicon samples were prepared. Compared to tungsten, silicon fabrication processes are well developed and material price is also lower. It has been reported that materials behaviors at high temperature, such as surface diffusion, are showing universalities in solid materials with its homologous temperature, T_h. The homologous temperature is the ratio of absolute temperature to its melting temperature [81].

In this regards, firing tests conducted on silicon samples. The silicon micro-trench was fired for 25 hours at 850 °C (T_h = 0.67), see Figure 3.14, and submicron holes array on silicon

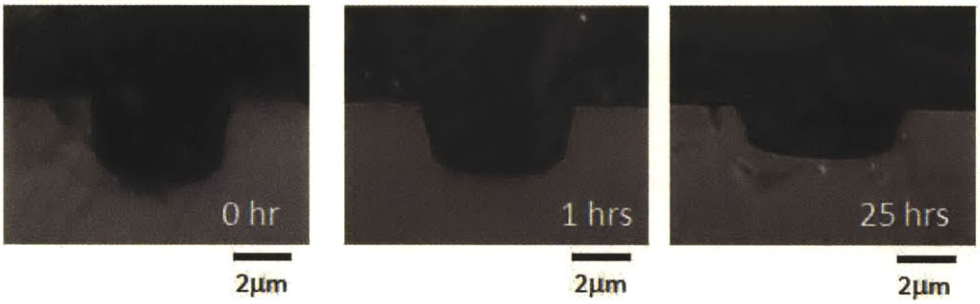

Figure 3.14 Cross-sectional SEM images of fired silicon samples: fired at 850 °C (T_h = 0.67), images taken at 0 hour, 1 hour, and 25 hours later. Nitrogen flow rate was 5 sccm, and ramp up and down rates were 3 °C/min.

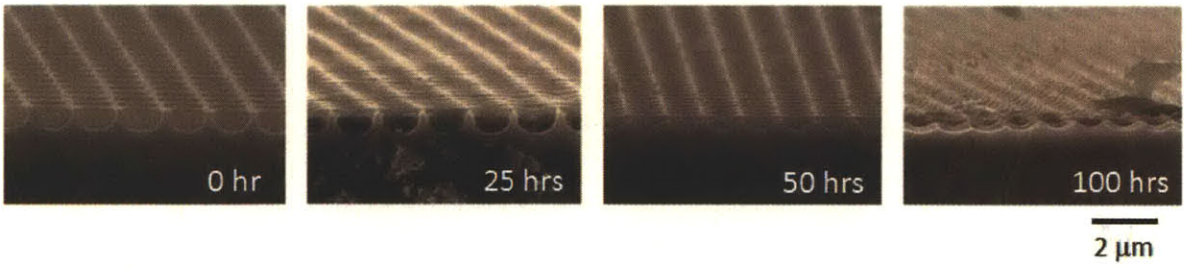

Figure 3.15 Cross-sectional SEM images for submicron-sized silicon hole arrays: fired at 400 ^{o}C (T_h = 0.40), images taken at 0, 25, 50, and 100 hours later (zoomed-in images are in Chapter 5. Nitrogen flow rate was 5 sccm and ramp up and down rate were 3 °C/min).

was fired for 100 hours at 400 °C (T_h = 0.4), see Figure 3.15. In both cases, the width (radius) increased and the depth got shallow with time. Based on the modeling and simulation, we brought the parameter, h/r, which is the ratio of the depth of the hole to the radius (or half of the width for 2-D). This h/r is decreased dramatically initially and saturated after 100 hours, Figure 3.16 (a). The measured values of h/r and normalized values for comparison are well matched with the model, see Figure 3.16.

3.4. Evaporation

The final mechanism of surface evolution is evaporation and condensation. At high temperatures, the amount of material that is vaporized from a solid surface can be significant. This "gas" creates a locally high vapor pressure and re-deposits on the surface nearby. This phenomenon was separately investigated with surface diffusion by preparing partially coated samples. Firing tests, similar to surface diffusion, were performed with single crystal silicon with a micro-meter scale trenches. However, for this, TiN diffusion barriers coated on the side-wall

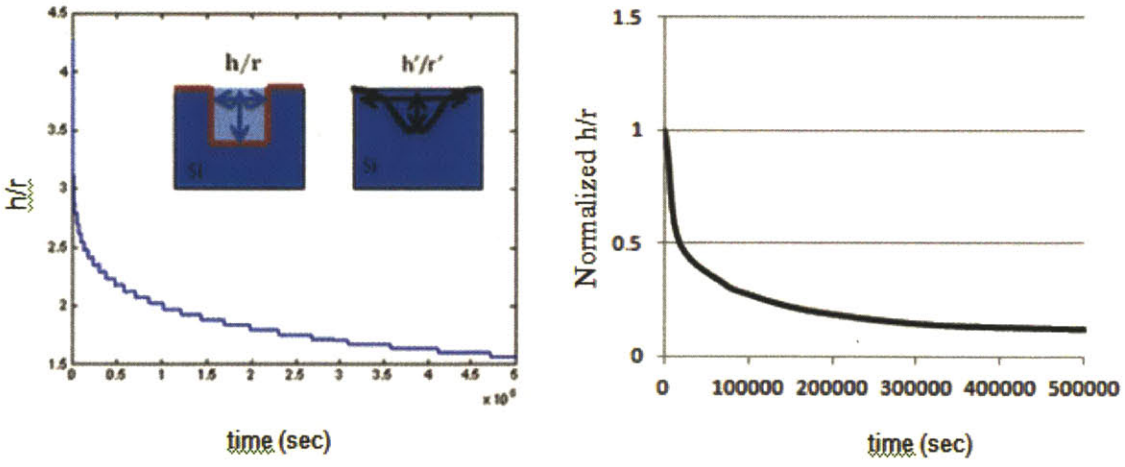

(a) (b)

Figure 3.16 (a) height-to-radius ratio (h/r) with respect to time by surface diffusion modeling for tungsten at 1200 °C (T_h = 0.40) and (b) normalized height-to-radius ($\frac{h/r}{h_o/r_o}$) from measured data from submicron silicon holes at 400 °C (T_h = 0.40), see Figure 3.15.

and bottom of the trenches. Top surface is originally coated with TiN but this layer was polished out by mechanical-chemical polishing. To make the same condition with previous surface diffusion test, the sample was heated to 850 °C and left for 100 hours, Figure 3.18. As seen in Figure 3.17, the width does not change much as it had before, see Figure 3. 14. These two samples were analyzed for height-to-width ratio. Interestingly, the coating on the side-wall and bottom reduced the geometry loss by evaporation. Since the test setup included flowing a large amount of forming gas to prevent oxidation, it was very hard to observe the re-condensation phenomena. Figure 3.18 shows the difference in changing height to width ratio. The difference between these two lines is the result of evaporation. Dashed line represents normal degradation by surface diffusion and evaporation. Solid line represents the degradation only by surface diffusion.

In *Kinetics of Materials*, R. W. Balluffi et. al. show how the normal surface velocity (v_n) that results from this redistribution of material is, in general, proportional to the curvature of the surface (K) and the ambient (non-local) vapor pressure (P_{amb}) of the material [82]:

$$v_n = AP_{amb}K \tag{3.3}$$

Depending on the application, this material flux may be controlled by lowering the ambient vapor pressure. Knowledge of this vapor pressure and the various elements that make up the constant of proportionality are required to determine the relative importance of condensation and evaporation . Also, it needs to be estiblished to know that diffusion barrier on the surface effectively prevents evaporation.

In detail, the normal velocity of the surface by which evaporation and re-condensation is derived, too:

$$v_n = -\frac{A\Omega^2\gamma P_{eq}}{kT}K \tag{3.4}$$

where, A is a vapor transport rate constant, P_{eq} is the vapor pressure in equilibrium with a local region of the surface with zero curvature, k : Boltzmann constant, T: absolute temperature, and K: curvature.

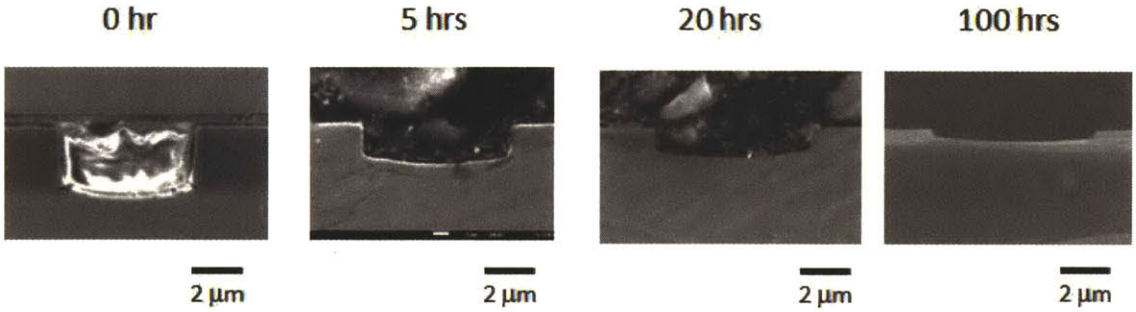

Figure 3.17 Firing tests with micro-scale trench fabricated on single crystal silicon. For this sample, the side-wall and bottom surfaces were coated with 5nm TiN. The top surface was planarized with chemical-mechanical polishing. Firing temperature was 850 °C and nitrogen flow rate was 5 sccm. The ramp-up and ramp-down rates were 3 °C/min.

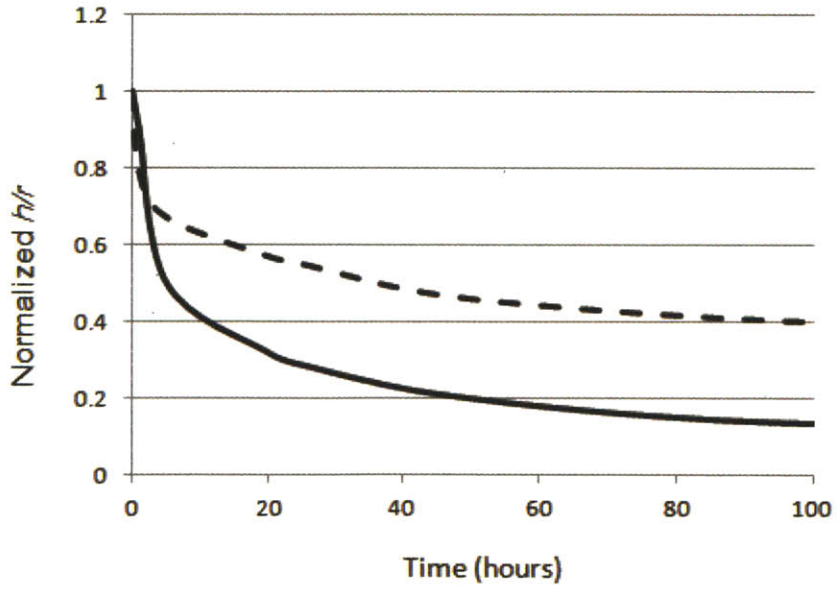

Figure 3.18: Height-to-radius ratio (h/r) versus time by surface diffusion modeling for silicon at 850 °C (T_h = 0.67). The dashed line represents degradation by surface diffusion and evaporation. Solid line represents degradation only by surface diffusion.

Chapter 4

Design and Solution

4. Proposed Solution for Long Term Thermal Stability of TPV Emitters

4.1 Design Idea

Through experiments, modeling and simulation, it has been found that four major modes of degradation of 2-D tungsten (or silicon) photonic crystal at high temperature: grain growth, oxidation, surface diffusion, and evaporation. The following ideas were suggested in the previous chapters for preventing the degradation of micro/nano-scale structure. First, grain growth or recrystallization can be avoided by using single crystal tungsten or by pre-annealing the polycrystalline sample before the fabrication of micro/nano-scale structures. Since surface diffusion occurs where a geometry has sharp curvature, a geometry of topographically flat but optically patterned surface will prevent the surface diffusion and evaporation. Thus, the second design idea which can prevent the surface diffusion is a flat surface photonic crystal (FSPC)*.

4.1.1. Flat Surface Photonic Crystal (FSPC)

Flat surface Photonic Crystal (FSPC) design is invented based on scientific/engineering analysis of fundamental sources of thermal degradation in micro/nano-scale structures. Surface diffusion and evaporation and re-condensation are unavoidable phenomena in micro/nano-scale structures at high temperatures. The governing equation of thermal degradation for each surface diffusion and evaporation and re-condensation depend on its material properties and its geometry. Recall the Equation 3.2 and Equation 3.4,

$$v_n = \frac{D_s \gamma \Omega^2 c_0}{kT} \frac{\partial^2 \mathrm{K}}{\partial s^2} \tag{4.1}$$

* US Patent pending: application number 61/563,396

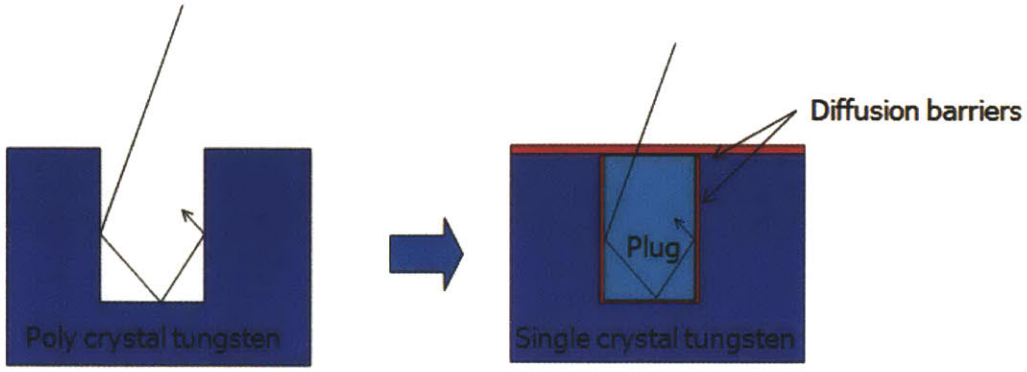

Figure 4.1 Conventional 2-D Photonic Crystal and the proposed design of Flat Surface Tungsten Photonic Crystal (FSTPC) Cross-sectional view for material description: First a thin inter-diffusion barrier is coated, then IR transparent ceramic is plugged, followed by (after flattening the surface by CMP) coating the surface with a thin layer of oxidation and evaporation barrier.

$$v_n = -\frac{A\Omega^2\gamma P_{eq}}{kT}K \tag{4.2}$$

At the certain temperature, material properties are not changes much, then the thermal degradation is dominant by geometrical factors, specially the curvature of the surface. Based on equations, if the curvature is zero, then there are no surface evolution by which surface diffusion or evaporation and re-condensation. FSPC design is based on the theoretical background of flat surface, zero curvature, will not have driving force for surface diffusion or evaporation and re-condensation.

This FSPC concept works under the assumption that the plugging material is optically transparent and the thin layer of inter-diffusion barrier and oxidation/evaporation barrier does not affect the optical performance of the device. Also, the material properties or geometry must be maintained at high temperature of TPV operation, 800 – 1100 °C. In Chapter 3, it has been observed that a thin layer of TiN coating followed by oxygen stuffing effectively prevents oxidation on the surface. However, oxygen stuffed TiN layer was not verified as an inter-diffusion barrier between plugged ceramic and tungsten. Also, the optical transmittance of plugging material must be tested by measuring its transmissivity for proving the concept.

4.1.2. Inter-diffusion Layer

An effective diffusion barrier between a metal and a ceramic plug would maintain the structure and its photonic crystal properties. The diffusion barriers reduce losing its selective optical property by inhibiting diffusion of substrate elements (such as Si, Ta, and W) into the ceramic material, and prolong the corrosion and oxidation resistance.

In this study, oxygen stuffing method along with TiN coating was used. Since the TiN film has a columnar structure, atoms can travel through the gap between the grains. Oxygen stuffing is the method to fill these gaps with oxygen molecules. This stuffing can be done by breaking the vacuum just after sputtering TiN film to allow the oxygen penetrate into the gap and fill the grain boundaries. Another method is to heat up the sample to 300 - 400 ^{o}C for 30 minutes to allow oxygen to fill the gap by being partially oxidized as TiON.

Since the transmissivity is inversely proportional to the thickness of the opaque material, the lesser the thickness of inter-diffusion barrier layer is, the lesser the radiation loss would be. Thus 5-7 nm of TiN was deposited for both inter-diffusion and evaporation barrier. Later in Chapter 5, the energy dispersive spectrometer (EDS) x-ray images to diagnose the penetration of material through this inter-diffusion barrier are presented.

4.2. Material Selection

4.2.1 Tungsten photonic crystals

To achieve the FSPC, the most important consideration is material selection. The criteria for material selection are that: the material has to be transparent at the wavelength below infra-red; the structure has to survive at the elevated temperature over 800 ^{o}C; and, the structure has to be manufacturable with current processing techniques. Materials for high operation temperature and IR transparancy are listed in Table 4.1. Tungsten (W) is the most common choice for selective emitter due to its high operation temperature and selective emissivity property. To keep the IR transparent plug stays inside of Tungsten micro/nano-scale pits at high temperature, the thermal expansion coefficient (TEC) of plugging ceramic should have slightly higher value than that of tungsten. Maintaining compressive stress while it expands at high temperature will mechanically secure the plug and keep it inside. Therefore, for W photonic crystal, zirconia (ZrO_2) or hafnium oxide (HfO_2) can be selected as a plugging material.

If the hole is positively tapered, plug may pop out due to the interfacial stresses generated by the force on the plug with acting toward outside. Therefore, the holes on tungsten should have slightly negative-tapered side walls. The sub-micron scale scallops on the side-wall, which is the results of the deep reactive ion etching process (D-RIE), can naturally secure the plugs. If the thermal expansion coefficient of the plugging material is too high, too much compression stress may occur. Stresses distribution around the boundary of tungsten and zirconia at 1200 °C (top view) is obtained from Ansys programming, Figure 4.2 (a). The SEM image of scalloped side-wall by D-RIE on silicon trench is shown by Figure 4.2 (b).

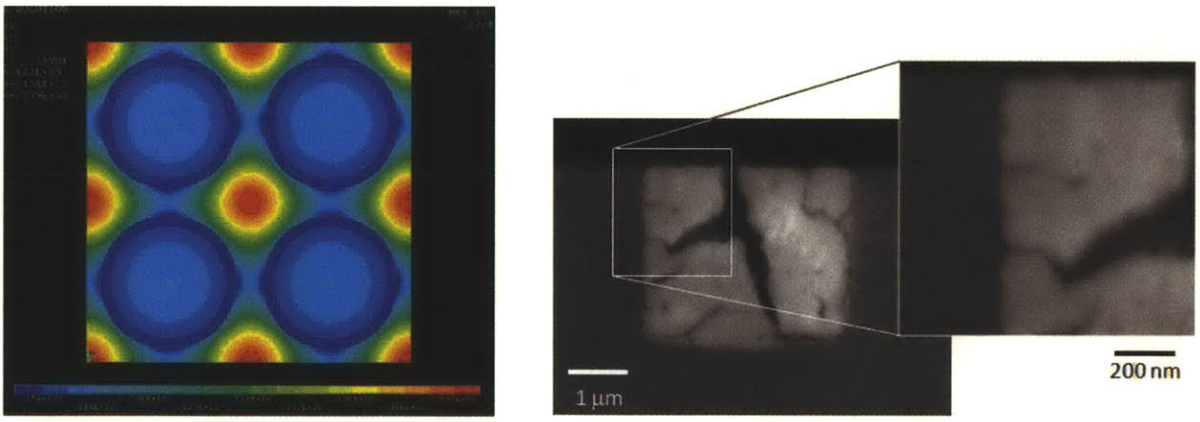

(a) (b)

Figure 4.2 (a) Analysis of the stress distribution when FSTPC is heated up to 1200 °C. Plugging material is Zirconia (ZrO_2) and the substrate is tungsten (W). At 1200 °C, 1540 MPa compressive stress at the boundary (sky blue), 1400 MPa compressive stress on Zirconia (blue), and 0 - 400 MPa compressive stress on Tungsten (green). (b) Scalloped side wall of the silicon trench. The image shows the plugged ZrO_2 but cracked. This issue is discussed in Chapter 5 (details process of parameters is in Appendix B).

Table 4.1: Properties of materials for FSTPC

Material	Melting Temp (°C)	Working Temp (°C)	TEC ($x10^{-6}$)	E (GPa)	Optical Properties
W	**3442**	**< 1700**	**4.3**	**411**	**Radiate**
Ta	3017	< 1375	6.3	186	Radiate
Si	**1414**	**< 1000**	**3.0**	**150**	**Radiate**
HfO_2	**2758**	**< 1500**	**5.9**	**220**	**0.25-10 mm Transparent**
ZrO_2	**2715**	**< 1500**	**10.3**	**200**	**0.3-7 mm Transparent**
SiC	2730	< 1650	4.0	410	Semi-Transparent
TiN	**2930**	**< 1500**	**9.3**	**251**	**Semi-Transparent**
Si_3Nx	1900	< 1200	3.3	310	Transparent RI=2.05
SiO_2	1600	< 1300	0.4	73	Transparent RI=1.46
MgO	2852	< 2000	8	295	Transparent

4.2.2. Silicon photonic crystals

Although tungsten is the most common material for selective emitter, micro fabrication techniques for tungsten are still under development and some of the firing tests require very high temperature. In order to prove the concept of FSPC, an alternative material, whose fabrication processes are well-developed and firing test conditions are much more favorable is chosen. From Table 4.1, silicon is the most common material for integrated circuits, and its fabrication process and equipment are proven by many other researches. Since silicon has a much lower melting temperature, the temperature required for accelerating test can be much lower than that of tungsten. Its lower thermal expansion coefficient also maintains the compressive stress at high temperature.

In this regard, silicon has been used for fabrication of the flat surface photonic crystal and tested with this sample to show the mechanical and optical performance at high temperature. A detailed study of the time-temperature relationship for different materials is described in Chapter 5.

4.3. Fabrication methods

After selecting the materials, manufacturability of the FSPC structure is another issue to solve. To achieve the structure in Figure 4.3 (a), the process flow for FSPC, Figure 4.3,is proposed. First, single crystal tungsten is prepared and drilled to have cylindrical micro/nano-scale trenches, and then a thin diffusion barrier layer is coated. An IR transparent ceramic is plugged and the surface is flattened by chemical mechanical polishing (CMP). Finally, the surface is coated by a thin layer of oxidation/evaporation barrier.

4.3.1 Fabrication method for plugging nano-pits

The most challenging part of the proposed processes is plugging the ceramic into the nano-pits. Initially, inkjet printing, spin coating, electroplating, and sputtering methods have been considered. Inkjet printing can be a good candidate for filling the holes due to its capability of generating pico liter droplets and it being free from the step-coverage issue from spin-coating or sputtering methods.

Spin coating is the most well-known process for zirconia coating on a flat surface, but the high step on the cylindrical holes may generate uneven stress at the corner which may results in cracks during annealing. Sputtering looks is promising process to maintain dense and uniform

coating over the whole area, but poor step coverage would result in incomplete filling of the holes. Electroplating or cathodic electrolytic deposition (ELD) was also considered but the inter-diffusion layer, TiN, has insufficient electrical conductivity and prevents ELD. To fill the micro-scale gap with ZrO_2 solution, the sol-gel method including a brushing step was modified. After spin coating the zirconia solution on the surface of the sample, the surface was brushed with a plastic Q-tip. In this process, additional zirconia solution fills the trench and excessive solution can be removed from the surface. In this way, the non-uniform stress distribution and cracking issue are solved during the pyrolysis process occurs. However, the results of annealing the sample for densification brought about the non-uniform stress distribution from the corners which resulted in the cracking of the plugged zirconia, Figure 4.4.

4.3.2. Challenges of Plugging

The most challenging process was filling the nano-pits with IR transparent, dense and crack-free ceramic. The source of cracking was non-uniform stress distribution from the surface, especially at the corners. Non-uniform thickness also results in cracking while annealing the ceramics, which is one of the typical failure modes of spin coatings on stepped structures.

While looking for the solution, a water-based solution coating method of ceramics was found. It is known that hydrolysis and condensation of metal species, while inhibiting the formation of large colloids, converted wet precursor coatings smoothly to dense films [83]. The precursor chemistry allowed a unique densification of the film and enabled to fabricate crack-free devices. Both ZrO_2 and HfO_2 can be coated by this method. From Table 4.1, I found that HfO_2 has a higher melting point and its thermal expansion coefficient is much less than that of ZrO_2. HfO_2, itself is also known as a common diffusion barrier material. However, just like other oxides, adhesion to metal is not strong, so the thin TiN layer can be used as an adhesion layer, Figure 4.5. Finally, the holes were successfully plugged with crack-free HfO_2, and the yield rate was above 90%, Figure 4.6 and Figure 4.7 (a), detail process flow and condition described on Appendix B).

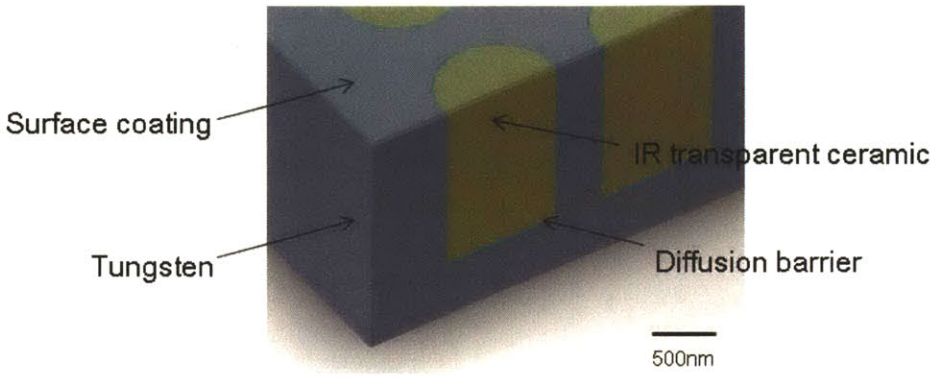

(a)

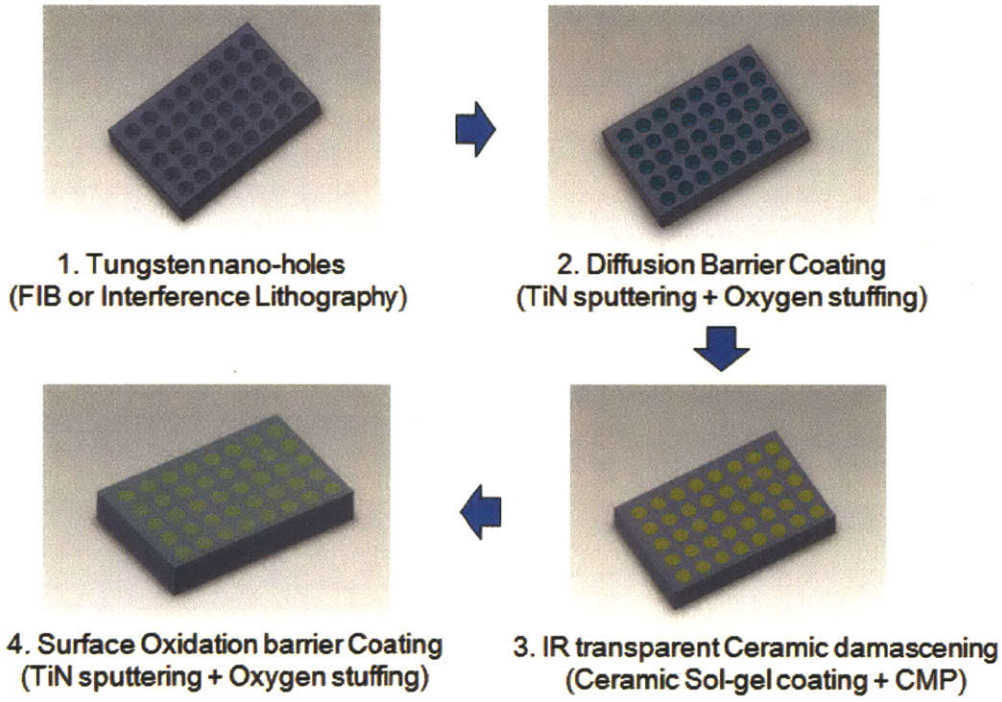

(b)

Figure 4.3 (a) 3-D schematic drawing of FSTPC and (b) process flow for obtain FSTPC. The concept and process is in pending patent, the U.S. application number is 61/563,396.

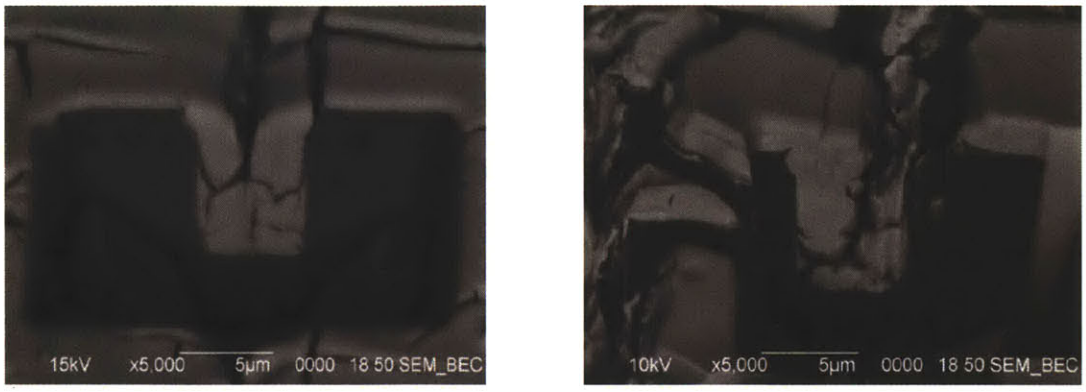

(a) (b)

Figure 4.4 Cracked ZrO_2 fills inside the silicon trenches after annealing at 650 °C for 2 minutes by rapid thermal annealing (RTA). The cross-section images were taken by focus ion beam, the large pocket milled and the samples were tilted by 52-degree for observation (the bright cracked area is zirconia and dark gray region is silicon).

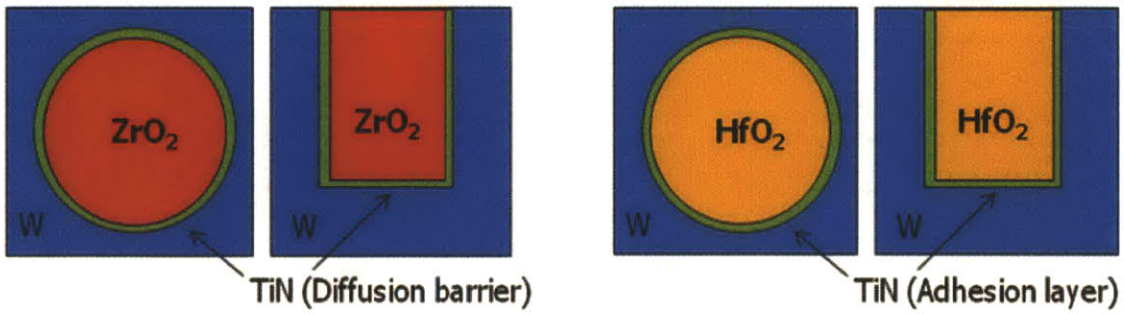

(a) (b)

Figure 4.5 Design change for crack free and denser plug: (a) original design with TiN inter-diffusion barrier and zirconia plug, (b) hafnium oxide (HfO_2) was chosen for filler material due to its higher melting temperature and lower thermal expansion coefficient than zirconia (ZrO_2). For (b), TiN layer can be thinner than previously and its role now is as an adhesion layer.

However there is another problem. The shrinkage in the thickness direction after final annealing is substantial, Figure 4.7 (b). The blue line on Figure 4.7 (b) represents the original si surface level. There was no crack generated inside the plugs but shrinkage along the longitude direction causes non-uniform thickness at the surface and detached plug from the bottom and side walls.

For solution based coating, the shrinkage happens after final annealing. Because of a single final annealing step at the end of the process, Figure 4.8 (a), a big shrinkage has occurred. After the process was modified with intermediate annealing steps, Figure 4.8 (b), the shrinkage problem was avoided, Figure 4.9.

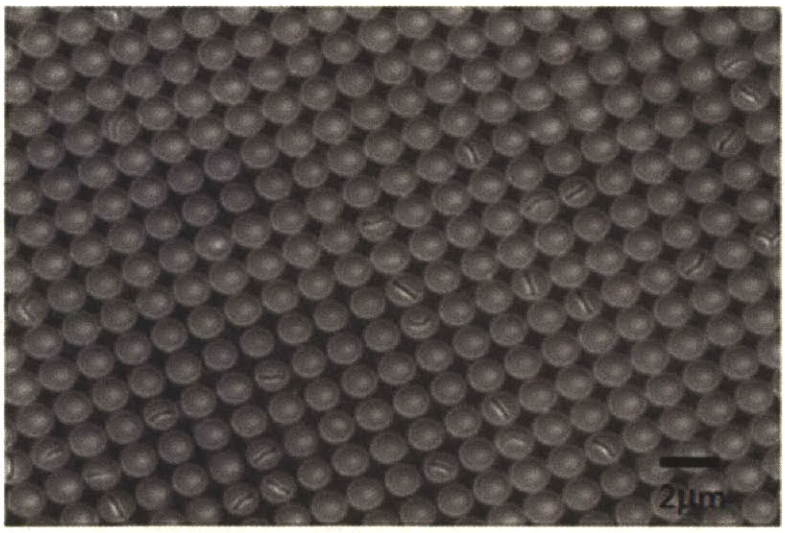

Figure 4.6 The yield rate was above 90%. Only 28 out 300 devices are cracked.

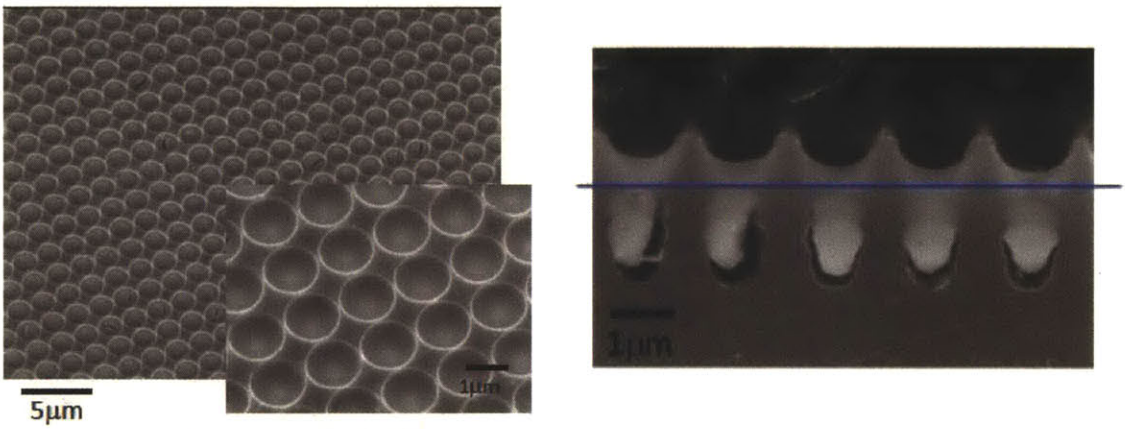

(a) (b)

Figure 4.7 (a) Crack-free HfO_2 coating on Silicon 2-D photonic crystal after annealing and (b) cross-sectional view of HfO_2 filled 2-D Si-PhC. The blue line is its original level surface. The shrinkage along the longitude direction was significant but no cracking on the plug.

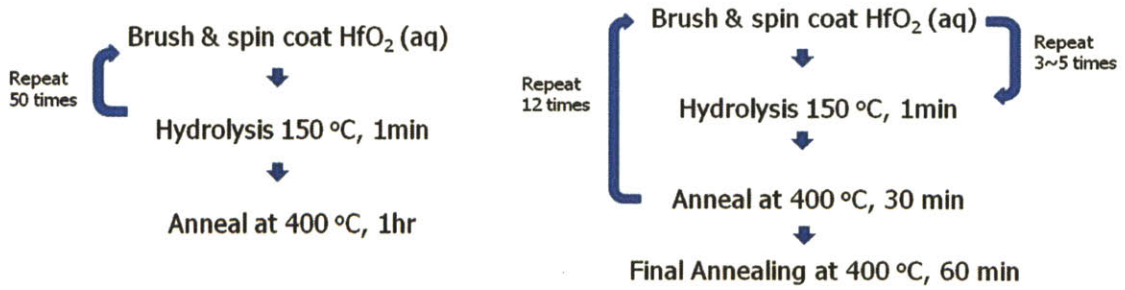

(a) (b)

Figure 4.8 (a) Original HfO_2 plugging recipe with huge shrinkage, only single final annealing step and (b) modified recipe to minimize shrinkage after annealing. Intermediate annealing steps are added

Chapter 5

Experimental Result and Discussion

5. Experiments

5.1. Accelerated Test Conditions

The goal of lifetime of FSPC emitters is over 30 years. To test designed device, accelerated tests is required for verifying the FSPC concepts. Not only with its accelerated test among the identical material, is the relationship among the materials at different temperature studied.

5.1.1. Based on activation energy (Arrhenius acceleration model)

The most frequently used acceleration model for diffusion and evaporation is the Arrhenius model, which assumes that the activation energy for each failure mechanism is unique and that every material has a constant value independent of temperature. The model equation is:

$$rate\ of\ degradation = A_o e^{-\frac{E_a}{kT}} \tag{5.1}$$

where *Life* (or rate of degradation) is the median life of a population, A_o is a scale factor determined by experiment, E_a is activation energy, k is Boltzmann's constant (8.62×10^{-5} eV/K), and T is temperature in Kelvin.

For silicon, the activation energy is $E_{a,Si} = 1.7\ eV/atom$, and that for tungsten is $E_{a,W} = 2.79\ eV/atom$. Based on Equation (5.1), after putting all the values for silicon at 850 °C and the equivalent temperature of tungsten is calculated to be 1570 °C. It means that for diffusion and evaporation, the degradation of identical geometry but for different materials can be calculated by comparing the values of activation energy. For the same amount of time, the degradation will be the same at 850 °C for silicon and 1570 °C for tungsten.

To obtain equivalent temperature, we need to modify Equation 5.1 with a surface diffusion formula, Equation 3.2:

$$v_n = \gamma\Omega^2 n \frac{D_s}{kT}\frac{\partial^2 K}{\partial s^2} = \gamma\Omega^2 n \frac{D_o e^{-\frac{E_a}{kT}}}{kT}\frac{\partial^2 K}{\partial s^2} = B_o \frac{e^{-\frac{E_a}{kT}}}{kT} \tag{5.2}$$

Since all the parameters remain the same, except the activation energy and temperature, similarly with Arrhenius acceleration model, the equivalent temperature for different materials for surface diffusion can be obtained. With this formula, the equivalent temperature for silicon at 850 ^oC is 1640 °C for tungsten.

Therefore, in this study, silicon sample at 850 °C were tested to investigate the thermal degradation effects which are equivalent for tungsten sample approximately at 1600 ^oC.

5.1.2. Homologous temperature (T_h)

Homologous temperature is the ratio of the absolute temperature of a material to its absolute melting temperature. It is expressed as:

$$T_h = T/T_m \tag{5.3}$$

It is well known that from various experimental data the material properties, such as tensile strength, shear strength and modulus of elasticity, of metal changes based on this homologous temperature for both poly- and single-crystalline materials.

For examples, creep, the tendency of a solid material to move slowly or deform permanently under the influence of stresses, occurs as a result of long term exposure to high levels of stress that are below the yield strength of the material. Creep is more severe in materials that are subjected to heat for long periods, and near melting point.

Recently, Flynn reported an interesting study regarding universality of surface diffusion by homologous temperature. His experiments that determine surface diffusion D_s on the close packed surfaces of vacuum compatible metals revealed that surface diffusion is approximately universal when scaled to homologous temperatures, T_h [81]. Similar behavior for vacancy-driven diffusion in bulk metals has been recognized, too.

This is an interesting result, because through this finding, the temperature acceleration tests among the different materials can be performed. It means that thermal degradation test by surface diffusion for tungsten at 1200 °C, homologous temperature T_h = 0.40), will show same surface diffusion with silicon at T_h = 0.40, which is 400 °C, which is much lower temperature. In this thesis, temperature acceleration tests (firing tests) based on Flynn's research were perfomed at a homologous temperature was 0.4.

5.1.3. Acceleration Factor

The Scale-accelerated failure time model (SAFT), which is also known as accelerated failure time (AFT) model, is a parametric model that provides an alternative to the commonly used proportional hazards models in the statistical area of survival analysis.

Under a SAFT model, lifetime at temperature *T*, *L(T)*, is scaled by a deterministic factor that might depend on temperature and unknown fixed parameters. More specifically, a model for the random variable *L(T)* is [84]:

$$L(T) = L(T_{use})/AF(T) \tag{5.4}$$

where the acceleration factor, *AF(T)* is a positive function of t satisfying $AF(T_{use}) = 1$. Lifetime is accelerated (decelerated) when $AF(T) > 1$ ($AF(T) < 1$).

For example, it the structure survived at T = 1200 °C for 100 hours, $L(1200°C)$ = 100 hours and the life time at 800 °C, L(800°C) can be obtained from the Equation (5.2). The acceleration factor for Arrhenius acceleration test can be obtained as[84]:

$$AF(T) = AF(T, T_{use}, E_a) = Exp\left(\frac{E_a}{k}\left(\frac{1}{T_{use}} - \frac{1}{T}\right)\right) \tag{5.5}$$

For prediction of the life time of designed and fabricated selective emitter, these equations are used and the result is shown in secssion 5.3.2

$$L(800°C) = L(1200°C) \times AF(1200°C) \tag{5.6}$$

$$AF(1200°C) = Exp\left(\frac{2.79}{8.617\times10^{-5}}\left(\frac{1}{1173.15}-\frac{1}{1473.15}\right)\right) = 3617 \quad (5.7)$$

5.2. Firing test of SiPhC

Before the crack-free plugging process was developed, firing tests we conducted at 850 °C. Total firing time was 100 hours, and scanning electron microscope (SEM) and electron dispersive scattering x-ray (EDS) images were taken at 0, 5, 20, 50, and 100 hours of ZrO_2 plugged silicon photonic crystal for analysis. With these experiments, it was expected to see that the oxygen stuffed TiN minimizes inter-diffusion and oxidation. Also, the flat surface design

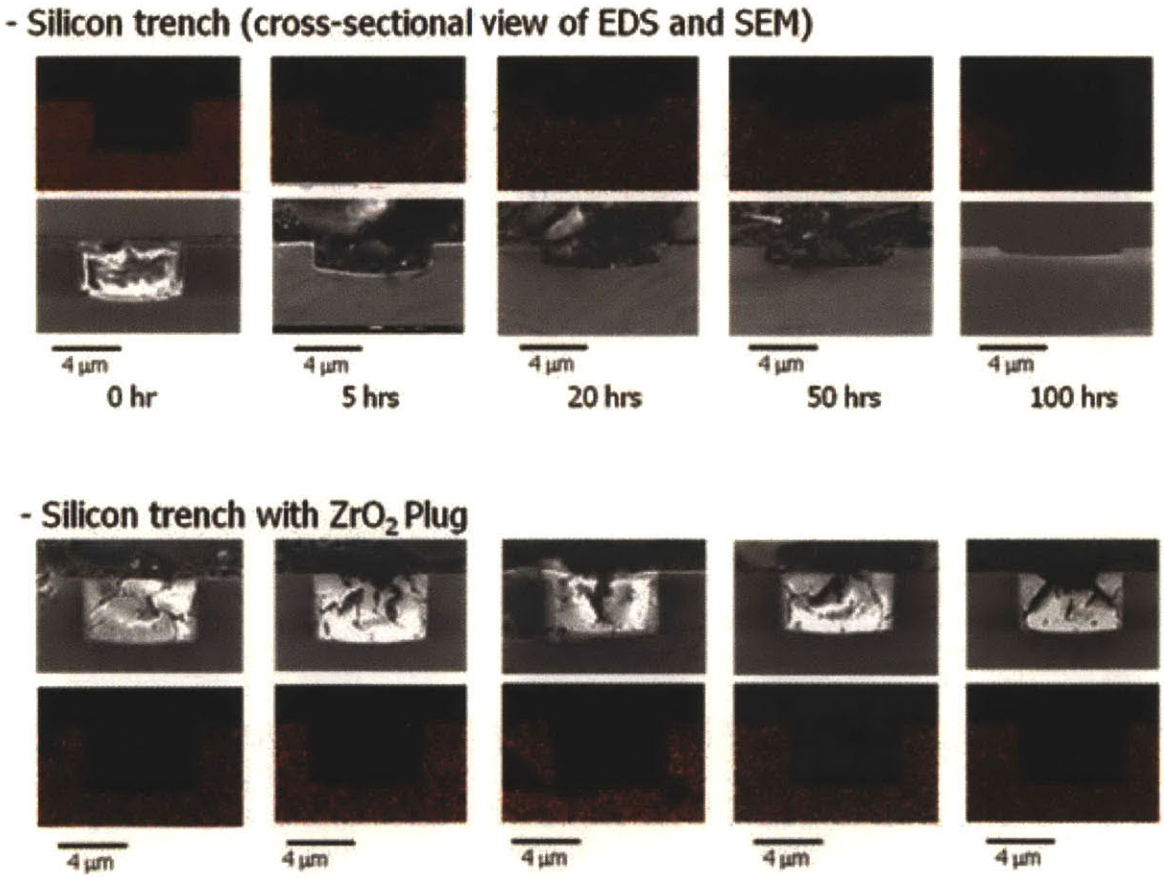

Figure 5.1: Firing tests with silicon micro trenches. ZrO2 plugged samples prepared by the proposed process of pattering, TiN coating, plugging, polishing, and another TiN coating. EDS images tracks the Si. Silicon-based flat surface design had a cracking issue but still provides the function of maintaining the physical structure. Nitrogen flow rate was 5 sccm and ramp up and down rates were 3 °C/min.

prevents surface diffusion and maintains its physical structures. By taking EDS images, Si was tracked along the interface between silicon-TiN-ZrO_2. As seen from ZrO_2 plugged trenches, Figure 5.1, there was no significant inter-diffusion observed with EDS even after 100 hours at 850 °C. SEM images and height-to-width ratio (Figure 5.2) also showed that plugged samples were maintained within less than 5 % range.

Therefore, the flat surface idea is a promising solution for the thermal degradation issue, but the scale is still in sub-micron level and the cracked plug may affect the optical properties of the device.

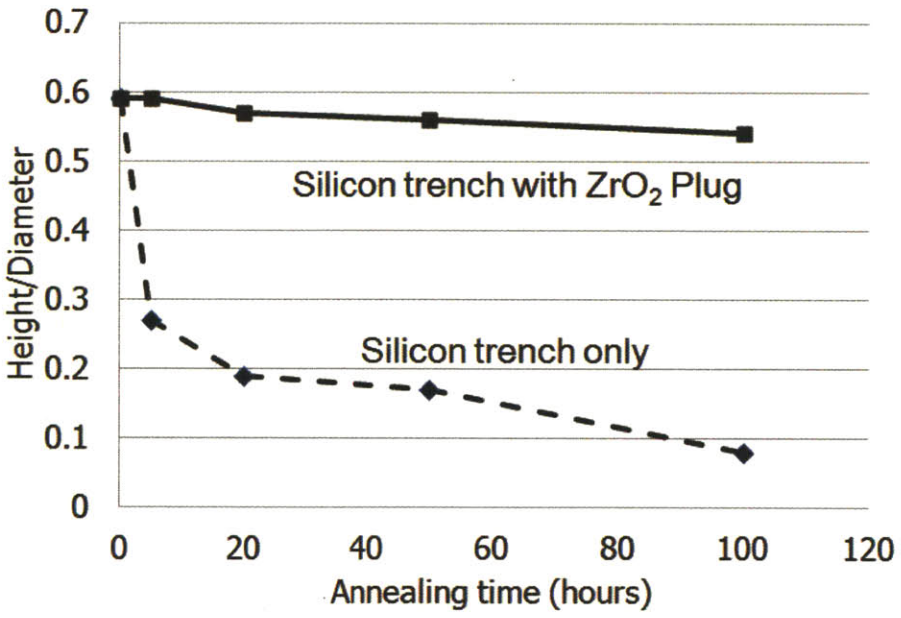

Figure 5.2: Height to width ratio with respect to firing time. While untreated silicon trenches degraded and changed the shape greatly, the plugged silicon trenches maintained the structure.

5.3 Optical Measurement of Flat Surface Silicon Photonic Crystal

5.3.1. Measurement system and Kirchoff's law

After proving the concept of flat surface design, which can prevent geometrical/thermal degradation, its optical performance was checked. First of all, the plugging material has to be transparent in the rage of application. Secondly, the emissivity of the samples has to be maintained after firing test.

To show theses two performances, a Fourier transform infrared spectroscopy (FTIR) for measuring emissivity with Kirchoff's law of radiation and incoming radiation equation was used. FTIR is a technique which is used to obtain an infrared spectrum of absorption, emission, photoconductivity or Raman scattering of a solid, liquid or gas [85]. An FTIR spectrometer simultaneously collects spectral data in a wide spectral range. In the present case, Kbr beam splitter and DTGS detector, which can measure optical spectra from approximately 1 μm to 5 μm were used. However, since at room temperature, the emission is too weak for detection, I called upon Kirchoff's law, which states "for opaque material, emission and absorption are equal at any wavelength and any phase [86]." Also, based on incoming radiation equation, "Incoming light consists of only absorptivity, reflectivity and transmissivity. From Equation 5.3, the emissivity can be obtained by measuring reflectivity and transmissivity.

$$\boldsymbol{\rho} + \boldsymbol{\alpha} + \boldsymbol{\tau} = 1 \tag{5.8}$$

The FTIR spectroscope can measure transmissivity and reflectivity at the same spot. I prepared two silicon photonic crystal samples, one is silicon photonic crystal and the other is HfO_2 plugged sample, which is made from the process introduced in Chapter 4. With simple emissivity measurement, we could see that the plugged sample, even without flattening the surface with polishing can have almost the same optical performance, Figure 5.3. That means the HfO_2 plug does not affect the optical property at wavelength range between 1 μm to 5 μm.

5.3.2. Optical performance along with the firing tests

These prepared samples were then fired at 400 °C (T_h =0.4) for 100 hours under 5 sccm of nitrogen flow. Cross-sectional images were taken with SEM and their emissivity measured with FTIR at 50 hours, 100 hours later. Figure 5.4 and Figure 5.5 show thermal degradation of silicon photonic crystal structure and corresponding images for flat surface HfO_2 plugged samples. As time goes, the holes depth is getting shallower while plugged samples remains its original geometry. It is more clear with zoomed-in images, Figure 5.5, that untreated samples approach its geometry to the flat surface by surface diffusion or evaporation and re-condensation.

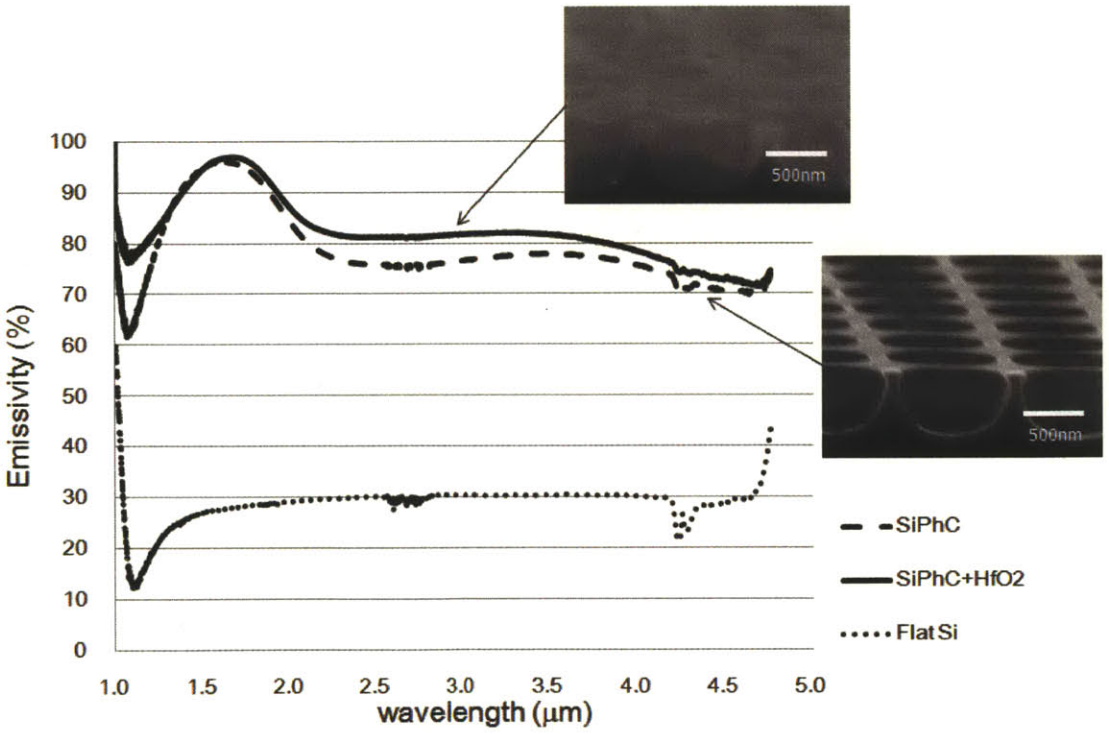

Figure 5.3: The effect of plugging HfO_2 on silicon photonic crystal. The emissivity difference is less than 5 % at wavelengths between 1 to 5 μm. Details of filter and detector selection and process condition are described in Appendix B.

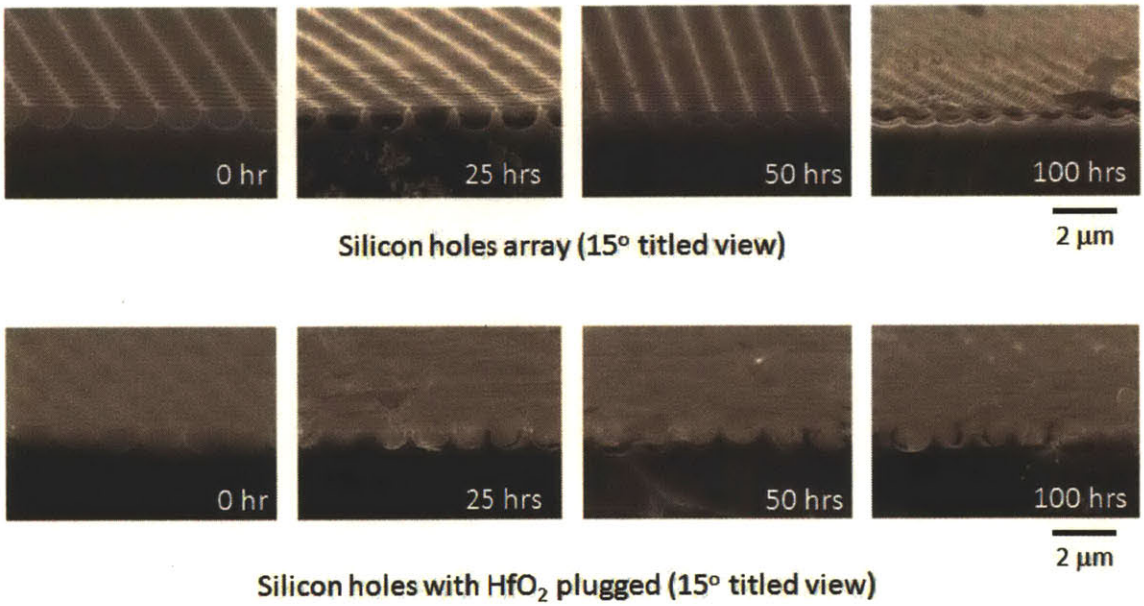

Figure 5.4: Thermal degradation of silicon photonic crystal structures and corresponding SEM images for HfO_2 plugged sample. Fired at 400 °C with nitrogen 5 sccm and ramp up and down rate were 3 °C/min.

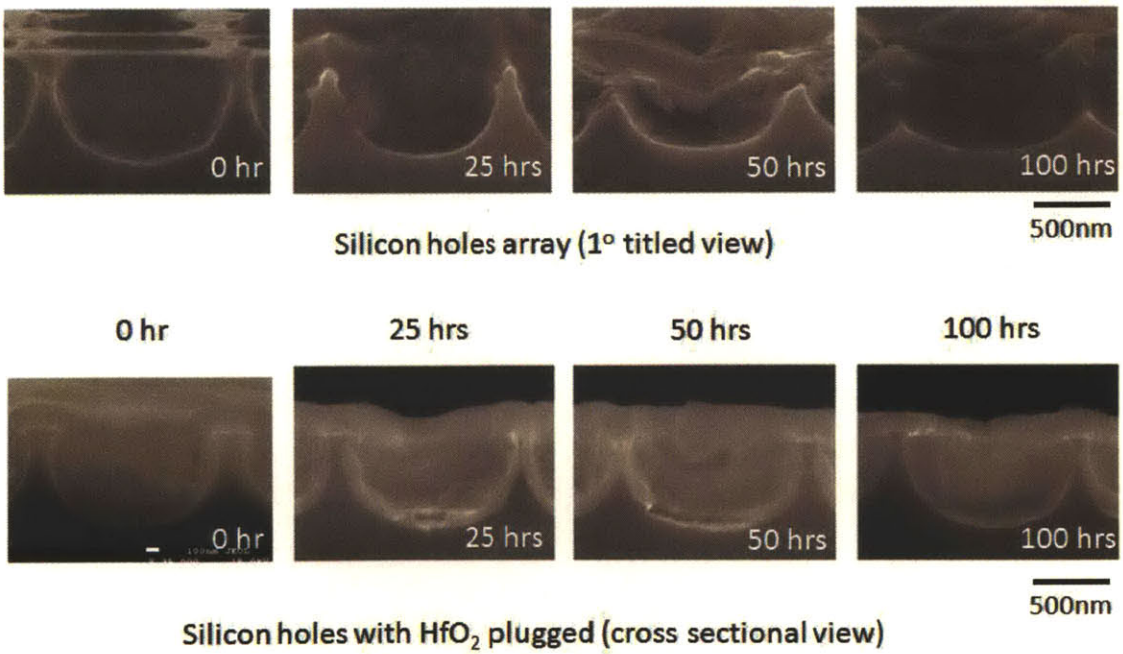

Figure 5.5: Cross-sectional view of thermal degradation of silicon photonic crystal structures and corresponding SEM images of HfO_2 plugged sample. Fired at 400 oC with nitrogen 5 sccm, and ramp up and down rate of 3 °C/min.

Finally, to examine the optical performance, the emissivity is measured for each sample after 0, 50, and 100 hours fired at 400 °C. As seen in Figure 5.6, the silicon photonic crystal emissivity curve decreases its emission as it degraded, and the emission curve approaches the flat silicon surface. By contrast, the HfO_2 plugged silicon photonic crystal does not lose its optical performance even after 100 hours of firing at 400 °C.

Therefore, at same T_h=0.4, 2-D tungsten photonic crystal can be survived at least 100 hours, which is equivalent temperature of 1200 °C and acceleration factor of AF(1200°C) = 3,612. From Equation 5.4, the life time of tungsten photonic crystal at 800 °C is at least 361,267 hours, which is approximately 41 years. If we use the same PhC at 900 °C, the life time will be at least 3 years.

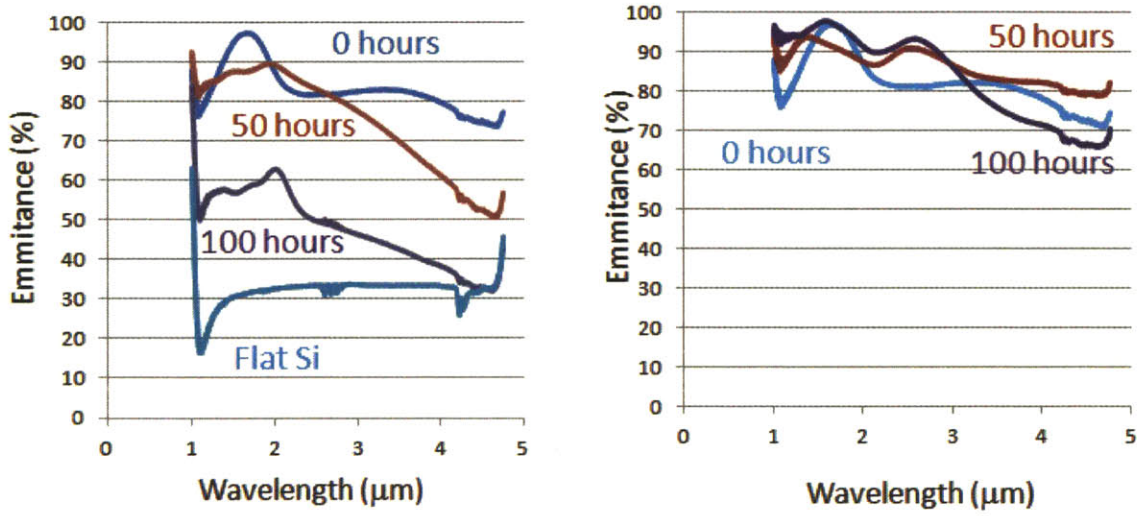

(a) (b)

Figure 5.6: Measured emissivity after 0, 50, 100 hours of firing test at 400 °C for: (a) silicon photonic crystal without any treatment (coating or plugging) and (b) HfO_2 plugged silicon photonic crystal sample.

Chapter 6

Conclusions

6. Conclusion and Future works

6.1. Summary of Accomplishments

Chapter 1 reviewed the currently available solar energy conversion systems focused on photovoltaic systems: p-n junctions, multi-junction, and other third generation PV cells. Their reported and theoretical conversion efficiencies are also presented. Among the third generation PV technologies, solar-thermophotovoltaic (S-TPV) system's concept is briefly introduced. Compared to multi-junction PV cells, the merits of S-TPV are presented: lower price materials, less complicated, easier fabrication process, and broader applications. However, the issue on S-TPV or TPV, thermal stability of 2-D selective emitters, is stated. Finally, the goal of this thesis, design and fabrication of thermally stable 2-D selective emitters was presented,

Chapter 2 focused on the literature of TPV energy conversion systems and their basic components: selective emitters (Photonic crystals) and PV diodes. A brief history of TPV was reviewed. The importance of spectral control and state of the art for high-efficiency are introduced. In more detail, the working principle, history, types of photonic crystals as selective emitters are presented.I concluded that 2-D photonic crystal is favorable in cost, manufacturing, and performance. However, for maximum efficiency, the 2-D photonic crystal must operate at very high temperatures, 800 – 1300 ^{o}C. Since, at such a high temperatures, micro/nano-scale structured 2-D photonic crystal cannot survive for a long time, the direction for solving this issue and a literature review on this specific issue were presented.

Chapter 3 presented a detailed investigation of four major modes of thermal degradation. Modeling, simulation, and experiments for these four major sources were investigated: grain growth, oxidation, surface diffusion, and evaporation. For each degradation mode, feasible solutions and tests are done. In detail, for the case of recrystallization and grain growth, pre-

annealing the substrate prior to micro/nano fabrication is proposed. If the selective emitters do not require large area, using single crystal tungsten can be a good choice. For oxidation, thin layer of TiN coating fellowed by oxygen stuffing was helpful to prevent or minimize the oxidation on the selective emitters' surface. Surface diffusion is unavoidable phenomena, but with having no curved surface, the source of surface diffusion can be fundamentally removed. Evaporation was also found by experiment and diffusion barrier coating method is proposed.

Chapter 4 provided the design guideline based on the findings of Chapter 3. The most challenging degradation mode was surface diffusion. To prevent surface diffusion, the structure should have optically periodic structure but it should be physically flat. To obtain this structure, plugging the nano-pits with optically transparent ceramic material, which has high thermal stability, is proposed. Next issue was oxidation. To minimize oxidation or evaporation, a diffusion barrier coating on top of the surface was proposed. This layer must be thin enough to pass the photons without losing its original energy but it must be thick enough to prevent oxidation or evaporation. For recrystallization issue, the substrate must be free from grain growth or recrystallization (single crystalline) or the grain size is already large enough (pre-annealed) so that the further grain growth may not affect much on the overall optical properties of selective emitters. A detailed design and fabrication of thermally stable structure, flat surface photonic crystal (FSPC), its fabrication process, and prepared samples were presented.

Chapter 5 mostly focused on proof of concept with experimental test. Both firing tests and optical measurement with fabricated samples were preformed. With these results, it may be concluded that ceramic plugged flat surface design with thin layer of inter-diffusion and oxidation barrier coated structure can guarantee significantly improved life time for 2-D selective emitters. Although the proof of concept of flat surface tungsten photonic crystal is done with different material, silicon, the relationship of time-temperature with different material based on activation energy and homologous temperature were useful tool for accelerated tests.

6.2. Suggestion for Future Studies

Since there are several limitations of fabricating tungsten photonic crystal, silicon 2-D photonic crystal was used for proving the concept for thermal stability. However, in real world application, the device is supposed to be made with tungsten. A general tungsten 2-D fabrication process is introduced in Figure 6.1. To generate micro/nano pattern, interference-lithography is

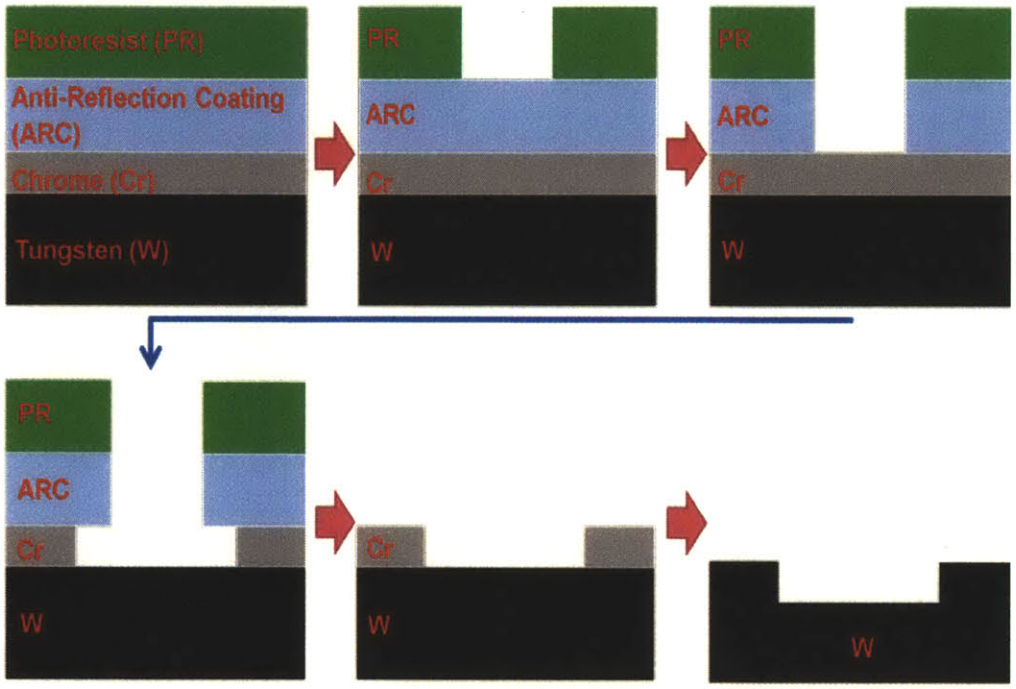

Figure 6.1: General process flow for 2-D tungsten photonic crystal. Bi-layer coating and hard-mask required for tungsten etching.

used. For this reason, bi-layer photo resist is required. The general process flow is depositing a layer of chromium (Cr) on the tungsten substrate, and then two lithography layers of anti-reflection coating (ARC) and photoresist (PR) coated on the chromium successively. After lithographic exposure, the desired pattern is transferred until periodic cylindrical holes on the W substrate are obtained [87].

However, this process includes wet etching of Cr, the final side-wall has very rough side wall. There have been attempts to solve this issue with high temperature etching of Cr, but still the wall roughness remains a problem, Figure 6.2.

Another issue is that by using interference-lithography, it can only generate square array holes of photonic crystal patterns. It is known that hexagonal array of the cylindrical holes array will give better control of emission selectivity [88]. In this regard, dry etching process or single step lithography may be required to improve the side-wall quality.

Thus, stepper lithography is suggested. The stepper allows up to five times image reduction ratio and the conventional minimum pattern width is about 2 μm, with up to 400 nm patterns on tungsten wafer. The most common issues for dry etching small samples are mounting and heating problem. Since the dry etching process is very sensitive to its substrate temperature during etching, mounting small samples on a standard size wafer, which is generally 6 inches, will have heat transfer problem and cause non-uniform etching throughout the process. Since the stepper also can generate the pattern in a small area, small samples using stepper will provide a single step of lithography process and avoid the heat transfer issue from dry etching.

Among high temperature transition metals, tantalum (Ta) recently received more interest since it has a higher melting temperature and is relatively cheaper than tungsten. Most of all, it has a much larger dry etching selectivity to photo resist (PR) compared with tungsten. The only consideration is that its thermal expansion coefficient is higher than HfO_2, Table 4.1. For the case of Tantalum (Ta), it is strongly suggested to using ZrO_2 as a plugging material. A water-based solution of ZrO_2 sol-gel can be prepared as the same method of HfO_2 water-based solution, Appendix B.

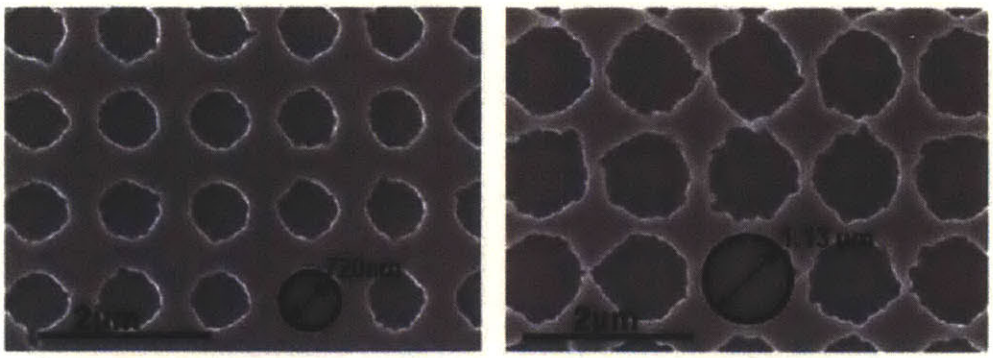

Figure 6.2: Wet etched chrome mask at difference etching times. It has very rough side-wall (SEM top view) [87].

Appendixes

Appendix A: Calculation of Radiative Power Flux (Emission)

(This work is done with Michael Ghebrebrhan)

```
;;2D planar tungsten slab
;;a in units of micron (i.e. a = 1um)

(define-param a 1)
(set-param! resolution 40)
;(set! Courant 0.25)
(use-output-directory)
(define-param normalization? true)

(define-param Lx 1.6)
(define-param Ly 15)
(define-param dpml 1.0)
(set! geometry-lattice (make lattice (size Lx Ly no-size)))
(set! pml-layers (list (make pml (thickness dpml) (direction Y))))

;; Tungsten LD data from Adrian
(include "../material-epsilon.ctl")
(set! extra-materials (list tungsten-epsilon))
(define-param d 3)  ;;;slab thickness
(define-param slab-center (/ (+ 2.56 -1) 2)); (- (/ Ly 2) dpml 1.0 (/ d 2)))
(define-param hole-depth 2.1)
(define-param hole-width 0.9)
(define-param hole-center (- slab-center (/ d 2)))  ;;placed at surface of slab b/c hole is defined to
have double its height

(if normalization?
   (set! geometry (list (make cylinder (center 0 0 0) (radius .1) (height infinity)
                              (material (make dielectric (epsilon 1.01)))))))

(define-param kx (/ 0.0 Lx))
(set! k-point (vector3 kx 0 0))

(define-param df (- 1 kx))
(define-param fcen (/ (+ 1 kx) 2))
(define (planewave-amplitude r)
  (make-polar 1 (* 2 pi (vector3-dot (vector3 kx 0 0) r))))

(set! sources (list (make source
```

```
            (src (make gaussian-src (frequency fcen) (fwidth df)))
            (component Ez) (center 0 (- (/ Ly 2) dpml 2) 0) (size Lx 0)
                (amp-func planewave-amplitude))))

(define file-a (open-input-file "f10000-a.txt"))
(define surface-list-x-a (list (read file-a)))
(define surface-list-y-a (list (read file-a)))

(define file-b (open-input-file "f10000-b.txt"))
(define surface-list-x-b (list (read file-b)))
(define surface-list-y-b (list (read file-b)))

(define file-c (open-input-file "f10000-c.txt"))
(define surface-list-x-c (list (read file-c)))
(define surface-list-y-c (list (read file-c)))

(define echo-file-a
  (lambda (n)
    (if (eof-object? n)
        (print "This is only a test.\n")
        (begin
          (set! n (read file-a))
          (set! surface-list-x-a (append surface-list-x-a (list n)))
          (set! n (read file-a))
          (set! surface-list-y-a (append surface-list-y-a (list n)))
          (echo-file-a n))))
(echo-file-a 1)

(define echo-file-b
  (lambda (n)
    (if (eof-object? n)
        (print "This is only a test.\n")
        (begin
          (set! n (read file-b))
          (set! surface-list-x-b (append surface-list-x-b (list n)))
          (set! n (read file-b))
          (set! surface-list-y-b (append surface-list-y-b (list n)))
          (echo-file-b n)))))
(echo-file-b 1)

(define echo-file-c
  (lambda (n)
    (if (eof-object? n)
        (print "This is only a test.\n")
        (begin
          (set! n (read file-c))
```

```
        (set! surface-list-x-c (append surface-list-x-c (list n)))
        (set! n (read file-c))
        (set! surface-list-y-c (append surface-list-y-c (list n)))
        (echo-file-c n)))))
(echo-file-c 1)

(define (is-between-a px n)
  (if (and (< (list-ref surface-list-x-a n) px) (>= (list-ref surface-list-x-a (+ n 1)) px))
     n      (is-between-a px (+ n 1))))

(define (is-between-b px n)
  (if (and (< (list-ref surface-list-x-b n) px) (>= (list-ref surface-list-x-b (+ n 1)) px))
     n      (is-between-b px (+ n 1))))

(define (is-between-c px n)
  (if (and (< (list-ref surface-list-x-c n) px) (>= (list-ref surface-list-x-c (+ n 1)) px))
     n      (is-between-c px (+ n 1))))

(define (surface-builder-a p)
  (let ((idx (is-between-a (vector3-x p) 0)))
    (define yi (list-ref surface-list-y-a idx))
    (define yi+1 (list-ref surface-list-y-a (+ idx 1)))
    (define xi (list-ref surface-list-x-a idx))
    (define xi+1 (list-ref surface-list-x-a (+ idx 1)))
    (if (<= (vector3-y p) (+ yi (* (/ (- yi+1 yi) (- xi+1 xi)) (- (vector3-x p) xi))))
        tungsten-epsilon air)))

(define (surface-builder-b p)
  (let ((idx (is-between-b (vector3-x p) 0)))
    (define yi (list-ref surface-list-y-b idx))
    (define yi+1 (list-ref surface-list-y-b (+ idx 1)))
    (define xi (list-ref surface-list-x-b idx))
    (define xi+1 (list-ref surface-list-x-b (+ idx 1)))
    (if (<= (vector3-y p) (+ yi (* (/ (- yi+1 yi) (- xi+1 xi)) (- (vector3-x p) xi))))
        air tungsten-epsilon)))
(define (surface-builder-c p)
  (let ((idx (is-between-c (vector3-x p) 0)))
    (define yi (list-ref surface-list-y-c idx))
    (define yi+1 (list-ref surface-list-y-c (+ idx 1)))
    (define xi (list-ref surface-list-x-c idx))
    (define xi+1 (list-ref surface-list-x-c (+ idx 1)))
    (if (<= (vector3-y p) (+ yi (* (/ (- yi+1 yi) (- xi+1 xi)) (- (vector3-x p) xi))))
        tungsten-epsilon air)))

(if (not normalization?)
    (set! geometry (list (make block (center 0 slab-center 0) (size Lx 3.56 infinity)
```

```
                (material (make material-function (material-func surface-builder-a))))
            (make block (center 0 (/ (+ 1.116 -1) 2) 0) (size 0.74 2.116 infinity)
                (material (make material-function (material-func surface-builder-b))))
            (make block (center 0 (/ (+ 0.413 -1) 2) 0) (size 0.74 1.413 infinity)
                (material (make material-function (material-func surface-builder-c)))))))
(define trans (add-flux fcen df 400 (make flux-region (center 0 (+ (/ Ly -2) dpml 1)) (size Lx
0))))
(define refl (add-flux fcen df 400 (make flux-region (center 0 (- (/ Ly 2) dpml 1)) (size Lx 0))))
(if (not normalization?) (load-minus-flux "refl-flux" refl))
(run-sources+ 200
        (at-beginning output-epsilon)
        (at-time 1 (output-png Ez "-A $EPS -a green:0.7 -Zc dkbluered -S2"))
        (at-every 10 (output-png+h5 Ez "-A $EPS -a green:0.5 -Zc dkbluered -S2")) )
(if normalization? (save-flux "refl-flux" refl))
(display-fluxes refl trans)

(exit)
```

Appendix B: Fabrication Details

Appendix B.1 Preparing tungsten sample for firing tests

1. Poly-crystalline tungsten sheet (t = 0.3mm) prepared.
2. Cut is it as 10 mm by 10 mm by die-saw.
3. Mechanical polishing.
    a. 300, 500, 1200, 1500, 4000
4. Focused Ion Beam Milling (beam size 11, 20 dose with Joel 4600F).
5. AJA sputter- TiN coating.
    a. Titanium Source *with Argon and nitrogen flow (5:7).
    b. 250V (300W).
    c. 5-7 nm (5 min, measured by quartz crystal reflectance).
    d. Oxygen stuffing: heating for 30 min in air at 300 °C (hot plate).

Appendix B.2 Silicon trench and silicon photonic crystal fabrication

1. N-type 2" silicon wafer prepared (t=0,35mm).
2. RCA cleaning.
3. HMDS, Spin coat photo resist (OCG 825), Soft baking for 30 minutes at 95 °C.
4. Lithography with MA6 (vacuum contact).
5. Develop resist with OCG 934 2:1 for approximately 90 seconds.
6. Rinse with Di-water, dry and hard backing at 95 °C for 30 minutes.
7. Wafer mount to 6" dummy wafer (back-side polished).
8. Asher for 2 minutes.
9. Deep-RIE for 2:30 min (MIT recipe name: MIT39 at STS3).
10. Piranha cleaning for detach wafer (immerse for 30 minutes).
11. Rinse with DI-water.

*Mask for micro-scale trench prepared with conventional e-beam method (thanks to Denis Ward at MTL).
**Mask for sub-micron scale photonic crystal prepared with the interference lithography (IL) method (thanks to Dr. Veronika Rinnerbauer).

Appendix B.3 HfO_2 water-based solution synthesis

1. $HfOCl_2 \cdot 8H_2O$ (Alfa Aesar, 98+%) dissolved in H_2O to a Hf concentration of 0.12M (2.457g of $HfOCl_2 \cdot 8H_2O$ dissolved in 50 mL Di-water for 0.12M of Hf).
2. 16.75 mL of 1M NH_3 (aq) (Mallinckrodt, ACS) added to the solution and stir vigorously until the pH reach 8.5.
3. Centrifuge the precipitates then wash with H2O to remove Cl^- and ammonia (5-6 times).
4. Check with $AgNO_3$ (aq) for no remained Cl^- and ammonia (until clear solution obtained with the precipitates).
5. Rinse 5-6 time with Di-water and collect precipitates.
6. 37 mL of 10M H_2O_2 (aq) (Mallinckrodt, ACS) and 8 mL of 2M HNO_3 (aq) (EDS, ACS) were added to the precipitates and stir for 12-24 hour.

Appendix B.4 HfO_2 plugging

1. Oxygen plasma at 10 mTorr, 5 sccm O_2, and 0.75 W/cm^2 for 10 minutes.
2. Spin coat the solution at 800-1000 rpm.
3. Swipe the surface with clean Q-tip.
4. Bake with hot plate at 150 °C.
5. Repeat step 2 to step 4 for five times..
6. Anneal with hot plate at 400 °C for 30 minutes.
7. Repeat step 5 and 6 until desired thickness is achieved.
8. Final annealing at 400 °C for 1 hour.

References

[1] A.E. Becquerel, C. R. Acad. Sci. 9 (1839) 145; A.E. Becquerel, C. R. Acad. Sci. 9 (1839) 561.

[2] C.E. Fritts, Proc. Am. Assoc. Adv. Sci. 33 (1883) 97; C.E. Fritts, Am. J. Sci. 26 (1883) 465.

[3] R.S. Ohl, Light-sensitive electric device, US Patent No. 2,402,622, 27th May 1941; R.S. Ohl, Light-sensitive device including silicon , US Patent No. 2,443,542, 27th May, 1941.

[4] http://www.greenrhinoenergy.com

[5] Shockley, W., and Queisser, H. J., 1961, "Detailed Balance Limit of Efficiency of P-N Junction Solar Cells," Journal of Applied Physics, **32**, pp. 510-519.

[6]http://rredc.nreal.gov/solar/spectra/am1.5/ Air Mass 1.5 Spectra, American Society for Testing and Materials.

[7] Green, M. A., Emery, K., Hishikawa, Y., Warta, W. and Dunlop, E. D. (2012), Solar cell efficiency tables (version 39). Prog. Photovolt: Res. Appl., 20: 12–20.

[8] N.V.Yastrebova (2007). High-efficiency multi-junction solar cells: current status and future potential.

[9] Timothy G. Gutowski, et al., 2011, "Thermodynamics and the Destruction of Resources," Cambridge University Press.

[10] Green, M. A., 2004, *Third Generation Photovoltaics: Advanced Solar Energy Conversion*, Springer, Berlin.

[11] Schaller, R. D., and Klimov, V. I., 2004, "High Efficiency Carrier Multiplication in Pbse Nanocrystals: Implications for Solar Energy Conversion," Physical Review Letters, **92**, 186601(1-4).

[12] Ross, R. T., and Nozik, A. J., 1982, "Efficiency of Hot-Carrier Solar-Energy Converters," Journal of Applied Physics, **53**, pp. 3813-3818.

[13] National Renewable Energy Laboratory (NREL), Golden, CO, July 2012 http://www.nrel.gov/news/press/2008/625.html.

[14] Swanson, R. M., 1979, "Proposed Thermophotovoltaic Solar-Energy Conversion System," Proceedings of the IEEE, **67**, pp. 446-447.

[15] Davies, P. A., and Luque, A., 1994, "Solar Thermophotovoltaics - Brief Review and a New Look," Solar Energy Materials and Solar Cells, **33**, pp. 11-22.

[16] V. Andreev, V. Khvostikov, and A. Vlasov, Chapter 9 Solar thermophotovoltaics, Springer Series in Optical Sciences, 2007, Volume 130/2007, 175-197.

[17] Jason Baxter, et all, " Nanoscale design to enable the revolution in renewable energy," Energy Environ. Sci., 2009,2, 559-588.

[18] Nils-Peter H. and Peter W., "Theoretical limits of thermophotovoltaic solar energy conversion," Semicond. Sci. Technol. 18 (2003) S151–S157.

[19] Martí, A., and Luque, A., eds., 2003, *Next Generation Photovoltaics: High Efficiency through Full Spectrum Utilization*, Institute of Physics, Bristol, UK.

[20] Dashiell, M. W., 2004, "Selection of the Ingaas/Inp as the Single Tpv Diode Material System for Research and Development," 2004 Direct Energy Conversion Program Review and Workshop

[21] Andreev, et al., 2007, "Solar Thermophotovoltaic Converters Based on Tungsten Emitters," Journal of Solar Energy Engineering-Transactions of the ASME, **129**, pp. 298-303.

[22] Nelson, R. E., 1995, "Thermophotovoltaic Emitter Development," The First NREL Conference on the Thermophotovoltaic Generation of Energy, AIP Conference Proceedings, 321, pp. 80-88.

[23] Bitnar, B., et all, 2002, "Characterisation of Rare Earth Selective Emitters for Thermophotovoltaic Applications," Solar Energy Materials and Solar Cells, **73**, pp. 221-234.

[24] Heinzel, A., et all,2000,"Radiation Filters and Emitters for the Nir Based on Periodically Structured Metal Surfaces,"Journal of Modern Optics, **47**, pp. 2399-2419.

[25] Martin, P. M., et all, 2002, "Sputtered Si: H Alloys for Edge Filters: Application to Thermophotovoltaics," Applied Optics, **41**, pp. 6702-6707.

[26] Hofler, H., Paul, H. J., Ruppel, W., and Wurfel, P., 1983, "Interference Filters for Thermophotovoltaic Solar-Energy Conversion," Solar Cells, **10**, pp. 273-286.

[27] Clevenger, M. B., Murray, C. S., Ringel, S. A., Sacks, R. N., Qin, L., Charache, G. W., and Depoy, D. M., 1999, "Optical Properties of Thin Semiconductor Device Structures with Reflective Back-Surface Layers," AIP Conference Proceedings, 460, pp. 327-334.

[28] Sulima, O. V., et al., 2001, "Fabrication and Simulation of GaSb Thermophotovoltaic Cells," Solar Energy Materials and Solar Cells, **66**, pp. 533-540.

[29] Zenker, M., et al., 2001, "Efficiency and Power Density Potential of Combustion-Driven Thermophotovoltaic Systems Using GaSb Photovoltaic Cells," IEEE Transactions on Electron Devices, **48**, pp. 367-376.

[30] Pan, J. L., et all, 2000, "Very Large Radiative Transfer over Small Distances from a Black Body for Thermophotovoltaic Applications," IEEE Transactions on Electron Devices, **47**, pp. 241-249.

[31] Whale, M. D., and Cravalho, E. G., 2002, "Modeling and Performance of Microscale Thermophotovoltaic Energy Conversion Devices," IEEE Transactions on Energy Conversion, **17**, pp. 130-142.

[32] Dimatteo, R., 2001, Presented at ONR/DARPA Direct Electrical Conversion Workshop, Alexandria, VA, December 4-5.

[33] R. E. Nelson, "TPV Systems and State-of-Art Development," *Proceedings 5th Conference on Thermophotovoltaic Generation of Electricity,* **653**, p. 3, September 2002.

[34] G. Guazzoni and S. Matthews, "A Retrospective of Four Decades of Military Interest in Thermophotovoltaics," *Proceedings 6th NREL Conference on Thermophotovoltaic Generation of Electricity,* **738**, p. 3, June 2004.

[35] H. H. Kolm, "Solar-battery power source," *Quarterly Progress Report, Solid State Research, Group 35,* MIT-Lincoln Laboratory, Lexington, MA, p. 13, May 1956.

[36] B. D. Wedlock, 1963, "Thermo-Photo-Voltaic Energy Conversion," *Proceedings IEEE,* **51**, pp. 694-698.

[37] David C. White, et al., "Recent Advance in Thermal Energy conversion," *Proceedings of the 15th Power Sources Conference,* pp. 125-132, May 1961.

[38] L.Fraas,et al., Proceedings of the 17th European Photovoltaic Solar Energy Conference, Munich, 2001.

[39] J.G.Cederberg, J.D.Blaich, G.R.Girard, S.R.Lee, D.P.Nelson, C.S.Murray,The development of(InGa)As thermophotovoltaic cells on InPusingstrain-relaxed In(PAs) buffers, Journal of Crystal Growth, 310(15), 2008, p3453–3458.

[40] C.A.Wang, H.K.Choi, D.C.Oakley, G.W.Charache, Recent progress in GaInAsSb thermophotovoltaics grown by organometallic vapor-phase epitaxy, Journal of Crystal Growth, 195, 1998. p346.

[41] I. Celanovic, F. O'Sullivan, M. Ilak, J. Kassakian, and D. Perreault, 2004, "Design and Optimization of One-Dimensional Photonic Crystals for Thermophotovoltaic Applications," Optical Letter, Vol. 29, No. 8, pp 863-866.

[42] E O'Sullivan, "Fabrication and Testing of an Infrared Spectral Control Component for Thermophotovoltaic Power Conversion Applications," M.S. Thesis, Department of Electrical Engineering and Computer Science, MIT, June 2004.

[43] R. E. Nelson, "Thermophotovoltaic Emitter Development," *Proceedings 1st NREL Conference on Thermophotovoltaic Generation of Electricity,* 1994.

[44] D. L. Chubb, "Reappraisal of Solid Selective Emitters," *Proceedings 21st IEEE Photovoltaic Specialists Conference,* 1990.

[45] I. Celanovic, et al., "ID and 2D Photonic Crystals for Thermophotovoltaic Applications," *Proceedings Photonics Europe 2004 Photonic Crystal Materials and Nanostructures,* International Society for Optical Engineering, vol. 5450, pp. 416, April 2004.

[46] N. Jovanovik, " Microstructured Tungsten Thermophotovoltaic Selective Emitters," Ph.D. Thesis, Department of Electrical Engineering and Computer Science, MIT, June 2008.

[47] M. Bianchi, C. Ferrari, F. Melino, A. Peretto, "Feasibility study of a TPV system for CHP application in residential buildings," Third International Conference on Applied Energy - 16-18 May 2011 - Perugia, Italy

[48] E. Palik, Handbook of Optical Constants of Solids, Academic Press, 1985.

[49] A. Licciulli, et al., "The Challenge of High-Performance Selective Emitters for thermophotovoltaic Applications," Semiconductor Science and Technology, vol. 18, pp. S174, April 2003.

[50] R. A. Lowe, et al., "Radiative Performance of Rare Earth Garnet Thin Film Selective Emitters," Proceedings 1st NREL Conference on Thermophotovoltaic Generation of Electricity, 1994.

[51] H. Yugami, "Thermophotovoltaic generation with surface grating selective emitters based on tungsten single crystals," Invited Presentation to the MIT Department of Mechanical Engineering, September 29, 2004.

[52] E. Hecht, *Optics,* Addison-Wesley, Reading, MA, 1998.

[53] http://en.wikipedia.org/wiki/Photonic_crystal

[54] E. Yablonovitch (1987), "Inhibited Spontaneous Emission in Solid-State Physics and Electronics," Physical Review Letters 58 (20): 2059–2062.

[55] S. John (1987), "Strong localization of photons in certain disordered dielectric superlattices," Physical Review Letters 58 (23): 2486–2489.

[56] J. W. S. Rayleigh (1888), "On the remarkable phenomenon of crystalline reflexion described by Prof. Stokes," Phil. Mag 26: 256–265

[57] E. Yablonovitch, T.J. Gmitter, K.M. Leung, E; Gmitter, TJ; Leung, KM (1991), "Photonic band structure: the face-centered-cubic case employing nonspherical atoms," Physical Review Letters 67 (17): 2295–2298

[58] Yablonovitch, Eli "Photonic Crystals: Semiconductors of Light", *Scientific American*, December 2001, accessed February 22, 2011.

[59] T. F. Krauss, R. M. DeLaRue, S. Brand (1996), "Two-dimensional photonic-bandgap structures operating at near-infrared wavelengths", Nature 383 (6602): 699–702.

[60] A. Narayanaswamy and G. Chen, "Thermal Radiation in 1D Photonic Crystals," Journal of Quantitative Spectroscopy and Radiative Transfer, Vol 93, 2005, pp. 175-18.

[61] M. Araghchini, Y. X. Yeng, N. Jovanovic, P. Bermel, L. A. Kolodziejski, M. Soljacic, I. Celanovic, and J. D. Joannopoulos, "Fabrication of two-dimensional tungsten photonic crystals for high-temperature applications". Journal of Vacuum Science and Technology. B Vol.29, No.6, 2011, p.061402

[62] T. Yoshie, J. Vuckovic, A. Scherer, H. Chen, and D. Deppe, "High quality two-dimensional photonic crystal slab cavities," Applied Physics Letter 79, 2001, pp.4289–4291.

[63] K. M. Ho, C. T. Chan, C. M. Soukoulis, "Existence of a Photonic Gap in Periodic Dielectric Structures," Phys. Rev. Lett., vol. 65, no. 25, December 1990.

[64] E. Yablonovitch, T. J. Gmitter, "Photonic Band Structure: The Face-Centered Cubic Case Employing Spherical Atoms," Phys. Rev. Lett., vol. 67, no. 17, October 1991.

[65] S. Y. Lin, et al., "A three-dimensional photonic crystal operating at infrared wavelengths," Nature, vol. 394, July 1998.

[66] S. Y. Lin, et al., "Enhancement and suppression of thermal emission by a threedimensional photonic crystal," Phys. Rev. B, vol. 62, no. 4, July 2000.

[67] J. Gee, et al., "Selective Emitters Using Photonic Crystals for Thermophotovoltaic Energy Conversion," Proceedings IEEE Photovoltaic Specialists Conference, 2002, pp. 896-899, May 2002.

[68] N.-P. Harder and P. Wurfel, "Theoretical limits of thermophotovoltaic solar energy conversion," Semiconductor Science and Technology, vol. 18, 2003, p. S151-S157.

[69] C. Henry, "Limiting efficiencies of ideal single and multiple energy gap terrestrial solar cells," J. Appl. Phys. 51, 1980, pp. 4494–4500.

[70] Peter Bermel et al., 2010 "Design and global optimization of high-efficiency thermophotovoltaic systems"Optics Express, **18**, No. 103,p A334.

[71] Lassner, Erik and Wolf-Dieter Schubert, 1999, "*Tungsten: Properties, Chemistry, Technology of the Element, Alloys, and Chemical Compounds*," New York, Kluwer Academic.

[72] C. Schlemmer, J. Aschaber, V. Boerner, and J. Luther, "Thermal stability of micro-structured selective tungsten emitters," *5th International Conference on Thermophotovoltaic Generation of Electricity*, 2003, pp. 164-173.

[73] K. Tosha, "Influence of pre-annealing on surface and surface layer characteristics produced by shot peening," Conf Proc: ICSP-8, 2002, Garmisch-Partenkirchen, Germany.

[74] C. R. Hammond (2004). *The Elements, in Handbook of Chemistry and Physics 81st edition*. CRC press.

[75] A. E. Kaloyeros and E. Eisenbraun, Annu. Rev. Mater. Sci. 2000. **30**, pp. 363–85.

[76] C.Y. Ting and M. Wittmer, Thin Solid Films, 1982, **96**, 327.

[77] W. Sinke and et all, Applied Physics letter, 1985, **47**, pp. 471-473

[78] W. Mullins, "Theory of thermal grooving," Journal of Applied Physics, **28**, 1957, pp. 333-339.

[79] Lassner, E., Schubert, W.D.,1999. Tungsten: properties, chemistry, technology of the element, alloys, and chemical compounds. New York: Kluwer Academic/Plenum Publishers.

[80] MIT MEEP, http://ab-initio.mit.edu/wiki/index.php/Meep

[81] Flynn CP., Why is diffusion in metals and on metal surfaces universal?, journal of Physics Condens Matter, 2006, **18**, S439-45

[82] Balluffi, R. W., Allen S. M., and Carter, W.C. (2005). Kinetics of Materials. Cambridge: Wiley.

[83] Kai Jiang, Jeremy T. Anderson, Ken Hoshino, Dong Li, John F. Wager, and Douglas A. Keszler, "Low-Energy Path to Dense HfO2 Thin Films with Aqueous Precursor," Chem. Mater, **23**, 945–952.

[84] Luis A. Escobar and William Q. Meeker, "A Review of Accelerated Test Models," Statist. Sci, **21**, Number 4 (2006), 552-577.

[85] Griffiths, P.; de Hasseth, J.A. (18 May 2007). Fourier Transform Infrared Spectrometry (2nd ed.). Wiley-Blackwell

[86] Guthrie, F. as Kirchhoff, G. (1860). "On the relation between the radiating and absorbing powers of different bodies for light and heat". Philosophical Magazine Series 4, **20**, pp. 1–21.

[87] M. Araghchini, "Efficient Silicon Micro-Reactors for Thermophotovoltaic Applications," E.E.D. Thesis, Department of Electrical Engineering and Computer Science, MIT, March 2011